the amount of material remaining after irradiation by the pump pulse. Thus, the proposed method provides a direct estimation of the excitation cross section.

2. Experimental setup

The MPI system consisted of two laser systems: one for the pump beam and one for the probe beam, synchronized by a pulse generator (DG645, SRS), as indicated in Fig. 1. The second harmonic of a Ti:sapphire laser (LT-2211, LotisTII) pumped by the second harmonic of an Nd:YAG (532 nm) served as the pump beam. The pump pulse was centered at 370 nm, with a bandwidth of 0.1 nm, a 10 ns full-width at half-maximum (FWHM), a repetition rate of 7 Hz, and pulse energy of 3.1 mJ. The laser beam was linearly polarized parallel to the electric field formed between the repeller (2.1 kV/cm) and the ground plate, which had a grid in the center to permit the flow of ions through the detector (see Fig. 1).

The probe beam consisted of the forth harmonic of a Nd:YAG laser (LT-2134UTF, LotisTII). The probe pulse was centered at 266 nm, with an FWHM of 5–6 ns, a 7 Hz repetition rate, and pulse energy of 0.21 mJ. The pulse beam was linearly polarized perpendicular to the electric field between the repeller and ground plate and arrived at the sample with an 80 ns delay with respect to the pump pulse.

The laser beams were spatially overlapped and focused into the ionization chamber by a fused-silica lens (focal length 300 mm). The spot size at the focal point of the pump beam was measured by a profile monitor (BC103, Ophir Optronics Ltd.), which yielded a $1/e$ radius at the beam waist of 73 μm (see Fig. 2). It was not possible to measure the probe beam with the profile monitor because its wavelength (266 nm) was beyond the range of the profile monitor. However, our time-of-flight (TOF) system is sensitive to position; hence, by comparing the 8-ns FWHM TOF distribution of iodine ions generated by the pump pulse to the 7-ns FWHM TOF distribution of iodine ions generated by the probe pulse, we estimated the radius of the probe-beam waist to be 59 μm.

To ensure the spatial overlap of the pump and probe beams at the sample position, we simultaneously observed MPI signals from the two pulses. To optimize the horizontal beam position, we adjusted the horizontal angle of the high-reflection (HR) guide mirror (see Fig. 1) while monitoring the TOF distributions by the oscilloscope. To optimize the vertical beam position, we adjusted the vertical angle of the HR mirror so as to minimize the number of parent ions generated by the pump pulse.

To change between pump–probe and probe-only mode, we used mechanical shutters, as shown in Fig. 1.

Ions produced by MPI were directed by a 2.1 kV/cm electric field into a 10 cm TOF tube, at the end of which, they were detected by a microchannel plate (MCP; F4655-10, Hamamatsu Photonics). The signals were transformed by a pump-triggered oscilloscope into TOF distributions, and averaged over 512 events were stored.

The sample material CH_3I (Wako Pure Chemical Industries, Ltd.) was kept in a glass cell cooled to the temperature of ice water. The vapor flow rate (0.19 atm. at 0 °C) into the vacuum chamber was controlled by a mass flow controller (M200S-TE07037, MKS). During MPI experiments, the CH_3I vapor pressure in the chamber was monitored by an ion gauge and maintained at approximately 1.3×10^{-4} Pa.

3. Principle of estimation

3.1. Enrichment factor

The sample vapor was contained in a glass cell and irradiated by UV laser pulses at frequent ~140 ms intervals. To achieve laser separation, we use the elimination method [31,32]. The pump pulse wavelength is tuned to excite the isotopic counterpart molecule ($^{12}CH_3I$) rather than the molecule of interest ($^{11}CH_3I$). The excited molecule then fragments, and the fragments are eliminated chemically. The number of counterpart molecules $[N_{12}(t)]$ obeys the rate equation

$$-\frac{d}{dt}N_{12}(t) = \eta \cdot N_{12}(t), \tag{1}$$

where η is the dissociation rate (s^{-1}). The solution to Eq. (1) is

$$N_{12}(t) = N_{12}(t=0) \cdot \exp(-\eta \cdot t). \tag{2}$$

In the present case, the dissociation rate of ground-state CH_3I approximately corresponds to the excitation rate because the inverse lifetime of the excited state that follows dissociation is

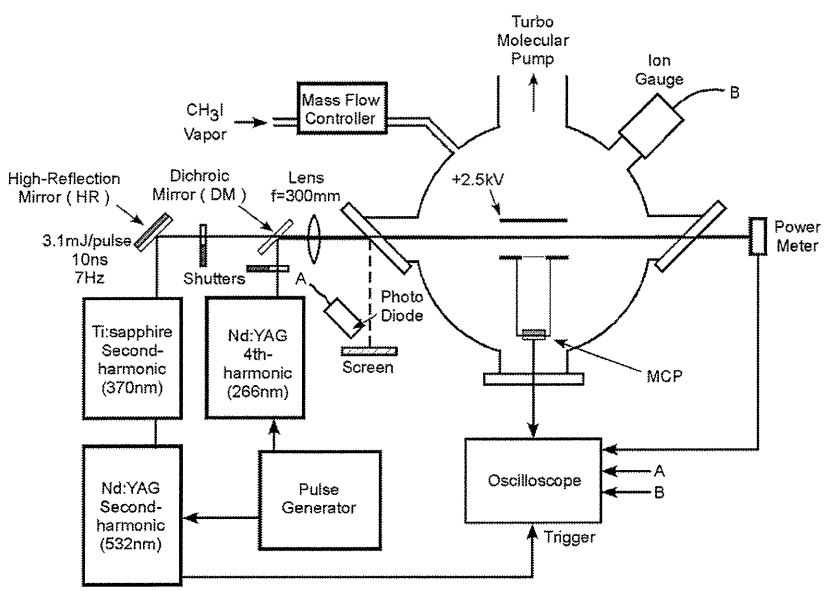

Fig. 1. Schematic of experimental apparatus, showing pulsed laser systems, system to synchronization pump and probe pulses, and the ion-detection system.

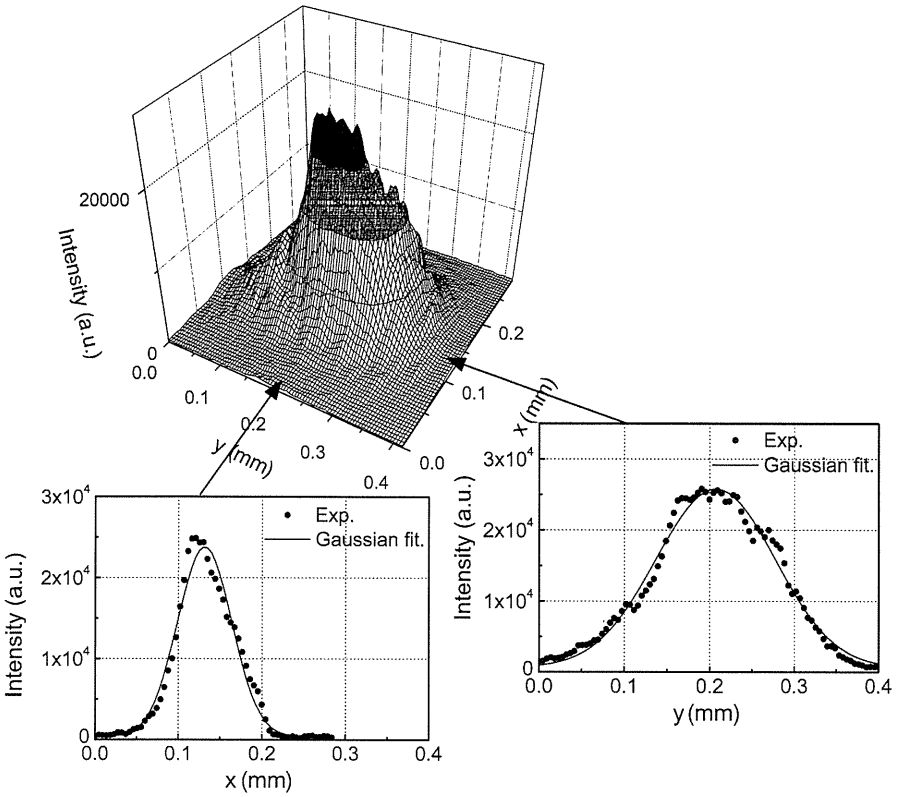

Fig. 2. Spatial profile of the pump pulse (370 nm) at the focal point. The beam focus elliptical. The $1/e$ radius of the profile was estimated to be 73 μm by averaging the y radius (major axis, 100 μm) and the x radius (minor axis, 45 μm).

significantly greater than the expected laser excitation rate (see Appendix A). Considering the laser reaction volume V into the cell volume V_C leads to the following dissociation rate:

$$\eta = \frac{V}{V_C}\sigma I, \tag{3}$$

where σ is the excitation cross section and I is the peak photon density delivered by the laser pump pulse ($cm^{-2}\,s^{-1}$). Using the number of dissociated molecules per pulse, the molecule density can be described by

$$N_{12}(n) = N_{12}(0)\exp\left(-\frac{V}{V_C}\sigma I\Delta t n\right). \tag{4}$$

For two-photon excitation, using the effective volume $V^{(2)}$ and the effective duration $\tau^{(2)}$ of pump pulse (see Appendix B), the number of the molecules can be described by

$$N_{12}(n) = N_{12}(0)\exp\left(-\frac{V^{(2)}}{V_C}\sigma^{(2)}I^2\tau^{(2)}n\right). \tag{5}$$

Using Eq. (5), the enrichment factor is given by [33,34]

$$\beta = \frac{N_{11}(n)/N_{12}(n)}{N_{11}(0)/N_{12}(0)} = \exp\left(\frac{V^{(2)}}{V_C}\sigma^{(2)}I^2\tau^{(2)}n\right), \tag{6}$$

assuming that $N_{11}(n) = N_{11}(0)$. Using Eqs. (B.9) and (C.1), the enrichment factor is

$$\beta = \exp\left(\frac{1}{2\sqrt{2}}\frac{V}{V_C}\sigma^{(2)}I^2\Delta t n\right). \tag{7}$$

For our purpose (i.e., CH_3I isotopic enrichment), we use the transition from the ν_3 vibronic state of the electronic ground state to the 6s Rydberg [3] state, which we call the "hot band" excitation (or the R 6s $3;3_1^0$ transition). That is, our target is the vibronic excited state of the molecule. Therefore, the number of real target molecules depends on the population of the ν_3 vibronic excited state. Considering the population ($b = 0.076$) of the ν_3 vibronic excited state at room temperature [35], the enrichment factor takes the form

$$\beta = \exp\left(\frac{1}{2\sqrt{2}}\frac{V}{V_C}b\sigma_{ex}^{(2)}(\nu_3)I^2\Delta t n\right) \tag{8}$$

where $\sigma_{ex}^{(2)}(\nu_3)$ is the two-photon-excitation of the hot band. This cross section is described in terms of the cross section $\sigma_{ex}^{(2)}$ of the transition from the electronic and vibronic ground states to the 6s Rydberg [3] state, (that is R 6s 3;0–0); $\sigma_{ex}^{(2)}$, as follows:

$$\sigma_{ex}^{(2)}(\nu_3) = f_{FC}\sigma_{ex}^{(2)}, \tag{9}$$

where f_{FC} is the Franck–Condon (FC) factor [36], which represents the overlap between the vibronic ground-state wavefunction and the ν_3 vibronic excited state wavefunction (single vibrational quantum). Substituting Eq. (9) in Eq. (8), the enrichment factor becomes

$$\beta = \exp\left(\frac{1}{2\sqrt{2}}\frac{V}{V_C}bf_{FC}\sigma_{ex}^{(2)}I^2\Delta t n\right) \tag{10}$$

In deriving Eq. (10), we assumed that the cell length in the beam direction is significantly less than the laser-beam focal length. Thus, the volume ratio approximately corresponds to the ratio of the cell window area to the cross-sectional area of the laser-beam waist, which we take as 1/4 in the present study. Therefore, for the laser to penetrate into the cell without distorting the laser profile, the radius of the cell window must be at least two times the radius of the beam.

It is apparent from Eq. (10) that accurately measuring the excitation cross section is essential to obtain a good estimate of the

enrichment factor. The photon density I and the laser pump pulse duration Δt depend on the laser system used.

Although we intended to measure the cross section of the hot band transition, the pulse power of our current laser system was insufficient to detect any dissociation effect based on the hot band transition. Therefore, we estimated the excitation cross section of the dominant ground-state transition, whose cross section is related to the cross section of the hot band transition by Eq. (9).

3.2. Signal reduction ratio

Fig. 3 shows an energy-level diagram of the ionization of methyl iodide CH_3I. The 370-nm pump-pulse wavelength yields parent and fragment ions from (2 + 1) REMPI via the 6*s* Rydberg [3] state, as shown in Fig. 3a. Actually, most excited molecules (>99.8%) dissociate into fragments (methyl radical and the excited iodine atom) within the pulse width Δt of our (pump and probe) laser pulses. The 266-nm probe pulse wavelength excites ground-state molecules to state A, which dissociate within 100 fs to neutral fragments [37], as shown in Fig. 3b. Subsequently, the fragments (CH_3 and I) are ionized by the same probe pulse [38,39].

The probe pulse probed the volume irradiated by the pump pulse, but with an 80 ns delay time, as indicated in Fig. 4. First, the pump pulse dissociates the CH_3I molecules within the volume V_U, which causes the molecular density within this volume to decrease. The density of the remaining molecules is monitored by the ion signals obtained from the probe pulse. The excitation cross section is obtained from the difference in the ion yields by the probe pulse with and without the pump (i.e., $\Delta Q = Q_{\text{pump on}} - Q_{\text{pump off}}$, where Q is the ion yield of the probe pulse).

In our experimental setup, the laser beam was focused at the cell by a convex lens to produce MPI within the sample. Thus, sample molecules within the laser-beam focal volume were ionized. Among the ions produced in this focal volume, only those within the beam axis length L_z corresponding to the detector diameter were detectable. Therefore, we considered the laser spatial distribution to be transverse Gaussian [$P(r/w)$, where w is the $1/e$ beam radius] and longitudinally uniform, as descried in Appendix B. In this case, by Eq. (B.7), the ion yields Q_B for the pump-off case are described by

$$Q_B = \rho \varepsilon_B^{(4)} I_B^4 \int P^4\left(\frac{r}{w_B}\right) 2\pi r dr L_z \tau_B^{(4)}, \tag{11}$$

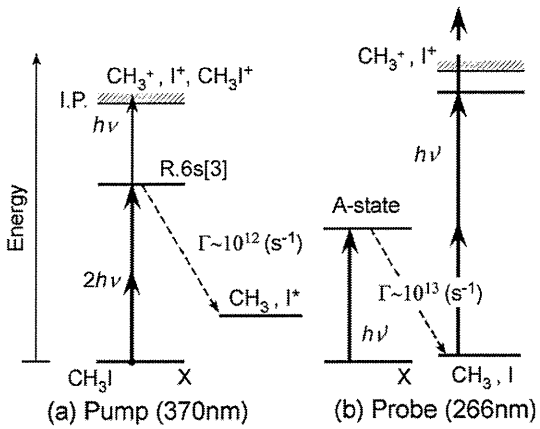

Fig. 3. Energy-level diagrams of CH_3I showing resonance levels relevant to the fragment- and parent-ion yields. (a) (2 + 1) REMPI via the R 6*s* [3] state, molecules excited to this state mainly dissociate to a neutral fragment, a methyl radical, and an excited iodine atom with a dissociation rate Γ. (b) MPI via state A. The fragments (methyl radical and iodine atom) dissociated from state A (lifetime ~100 fs [37]) are ionized by multiphoton absorption.

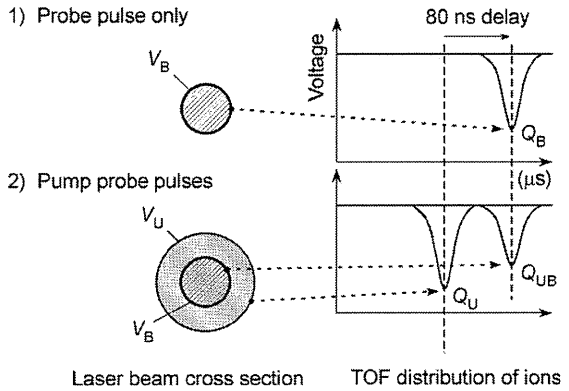

Fig. 4. Scheme to estimate the excitation cross section. The density of the target material decreases upon excitation by the pump pulse and subsequent dissociation. The decreased density leads to a reduction in probe-pulse ionization. V_U and V_B represent the reaction volumes of the pump and probe pulses, respectively.

and the ion yields Q_{UB} for the pump-on case are described by

$$Q_{UB} = \rho \varepsilon_B^{(4)} I_B^4 \int \left[1 - \sigma_{ex}^{(2)} I_U^2 P^2\left(\frac{r}{w_U}\right) \tau_U^{(2)}\right] P^4\left(\frac{r}{w_B}\right) 2\pi r dr L_z \tau_B^{(4)}, \tag{12}$$

where $\varepsilon_B^{(4)}$ is the ionization cross section of the probe pulse, and the subscripts U and B refer to the pump pulse and probe pulse, respectively. From Eqs. (11) and (12), the reduction ratio of the ion yields is

$$\frac{Q_{UB}}{Q_B} = 1 - \sigma_{ex}^{(2)} I_U^2 \tau_U^{(2)} \left(\frac{\int P^2\left(\frac{r}{w_U}\right) P^4\left(\frac{r}{w_B}\right) 2\pi r dr}{\int P^4\left(\frac{r}{w_B}\right) 2\pi r dr} \right). \tag{13}$$

Therefore, the reduction ratio of ion yields is given by

$$\frac{Q_{UB}}{Q_B} = 1 - \frac{\sigma_{ex}^{(2)} I_U^2 \tau_U^{(2)}}{\frac{S_B}{2S_U} + 1}, \tag{14}$$

where $S_U (= \pi w_U^2)$ and $S_B (= \pi w_B^2)$ are the cross-sectional areas of the laser-beam waist for the pump and probe beams, respectively. If we define the reduction ratio of the ion signal as

$$R_{rd} = \frac{Q_{UB}}{Q_B}, \tag{15}$$

the excitation cross section may be expressed as

$$\sigma_{ex}^{(2)} = \frac{1}{I_U^2 \tau_U^{(2)}} \left(\frac{S_B}{2S_U} + 1\right)(1 - R_{rs}). \tag{16}$$

Replacing the effective pump-pulse time $\tau_U^{(2)}$ with the actual time (Δt_U) by Eq. (C.1) gives

$$\sigma_{ex}^{(2)} = \frac{\sqrt{2}}{I_U^2 \Delta t_U} \left(\frac{S_B}{2S_U} + 1\right)(1 - R_{rd}). \tag{17}$$

We experimentally obtained the reduction ratio R_{rd} and used Eqs. (10) and (17) to estimate the enrichment factor.

Note that our method assumes that the fragments are not ionized by the probe pulse. We assume that the iodine atom that dissociates from the 6*s* Rydberg [3] state is excited to $I^*(^2P_{1/2})$ [40]. Unlike ground-state iodine, iodine in this excited state does not have a transition that is resonant with the probe-pulse photon energy. Detection of I^+ is suitable for our method. However, although the methyl radical is ionized by the probe pulse, it is released from the reaction volume with the kinetic energy of molecular dissociation. During the pump–probe delay time (80 ns), the methyl radical with a velocity of 4×10^3 m/s [41] travels approximately 0.32 mm, which is greater than the radius of the probe-beam waist. Therefore, most of the radicals are not irradiated by the probe pulse.

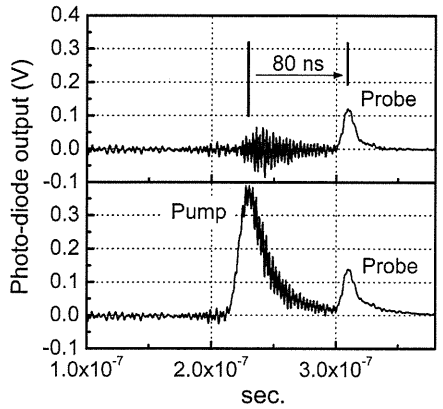

Fig. 5. Timing of two laser pulses using a photodiode detector. The probe pulse arrives at the sample 80 ns after the peak of the pump pulse. The ringing noise in the upper panel is attributed to the electrical noise caused by the flash pumping of the Nd:YAG gain medium in the probe laser. Because this noise disappeared when we stopped the Nd:YAG laser (probe pulse).

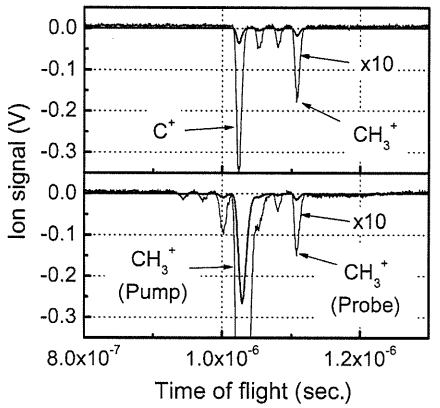

Fig. 6. Time-of-flight distributions of methyl radical ions generated solely by the probe pulse (upper panel) and by the pump and probe pulses (lower panel).

However, out of concern that the ionization of methyl radical fragments having flight paths parallel to the laser axis would distort the signal, we did not use data from the methyl radical ions to estimate the requisite cross section.

4. Results

The timing between the pump and probe pulses was monitored by a photodiode for both probe-only (Fig. 5, top panel) and pump–probe modes (Fig. 5, bottom panel). The pulse generator output reveals that the probe pulse followed the pump pulse. A ringing noise appeared before the probe pulse, but this noise disappeared when we stopped the Nd:YAG laser (i.e., the probe beam laser). Therefore, we attribute the noise to electrical noise generated by the flash pumping of the Nd:YAG laser gain material. Because of the insufficient bandwidth of our photodiode (cutoff frequency = 900 MHz), we consider that the actual width of the pump pulse is less than the 26 ns measured with our photodiode.

Fig. 6 shows the TOF distributions of the fragment ions (methyl radical ions). The upper panel shows results for the probe-only mode. The four peaks correspond to CH_n^+ ($n = 0, 1, 2, 3$). The last one of the four peaks corresponds to the methyl radical ion (CH_3^+). The lower panel shows results of the pump–probe mode. The largest peak in the lower panel corresponds to methyl radical ions (CH_3^+) generated by the pump pulse. The C^+ peak that appears in the upper panel overlaps temporally with the CH_3^+ peak generated by the pump pulse (lower panel). The methyl radical ion signal in the lower panel appears to be slightly smaller than that in the upper panel. From the magnitudes of these peaks, we estimated the reduction ratio of the methyl radical ions.

Fig. 7 shows the TOF distributions of iodine ions (I^+) and parent ions (CH_3I^+). The largest of the three peaks in the lower panel corresponds to iodine ions generated by the pump pulse, and the center of the three peaks corresponds to I^+ generated by the probe pulse. We can see that the I^+ peak in the lower panel (pump probe) is smaller than that in the upper panel (probe only). We attribute the decrease in the I^+ peak to the dissociation of methyl iodide molecules caused by the pump pulse. We estimate the reduction ratio of I^+ from the magnitude of these peaks.

The reduction ratios of the signals of the fragment ions (CH_3^+ and I^+) due to the probe pulse were calculated using Eq. (15) and are shown in Fig. 8. We observe a significant reduction of probe-generated ions, which we attribute to the depletion of the parent population caused by the pump pulse. The errors shown in the

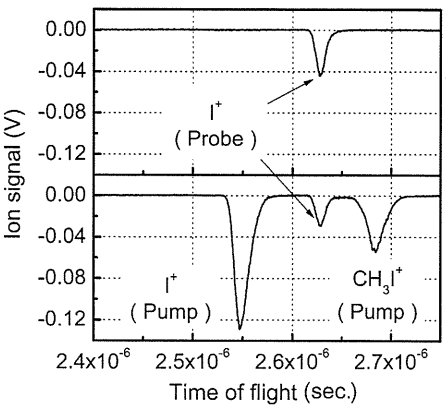

Fig. 7. Time-of-flight distributions of iodine ions and parent molecules generated by the probe pulse alone (upper panel) and by the pump and probe pulses (lower panel).

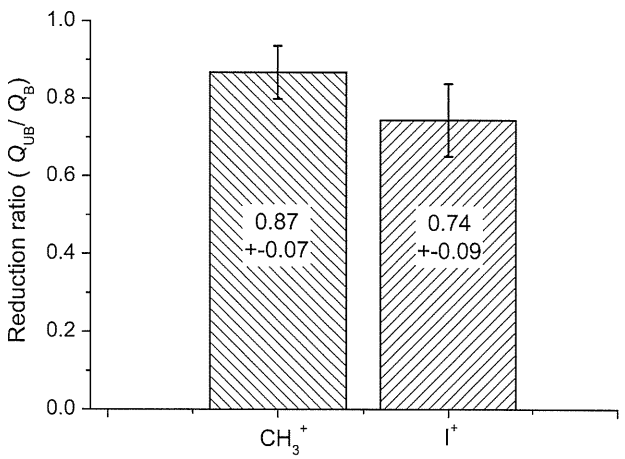

Fig. 8. Reduction ratio for ions fragmented by the probe pulse after irradiation by the pump pulse.

figure represent the standard deviation of our data (8 samples). To estimate the excitation cross section at the pump wavelength, we used the reduction ratio of 0.74 ± 0.09 for I^+. Then, by Eq. (17), we obtained the two-photon-excitation cross section of the R 6*s* 3;0–0 transition as $4.1 \pm 1.4 \times 10^{-48}$ (cm^4 s).

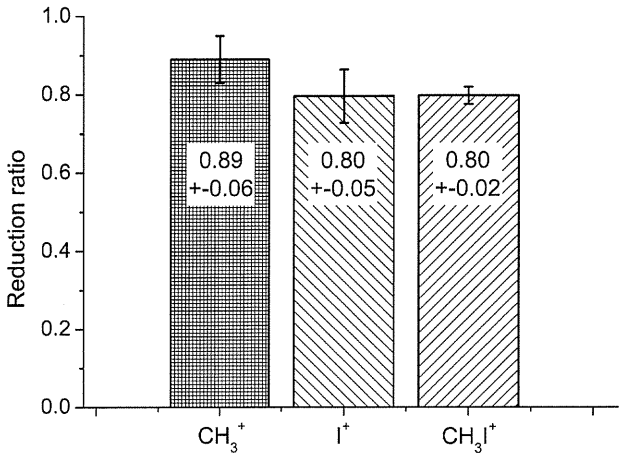

Fig. 9. Reduction ratio for fragment and parent ions generated by the probe pulse (370 nm) after irradiation by the pump pulse (266 nm).

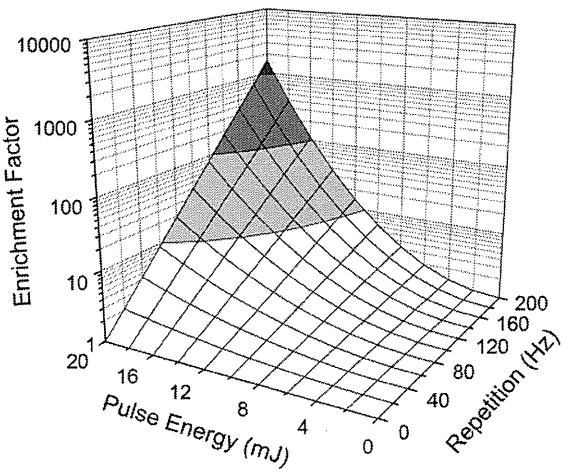

Fig. 10. Predicted enrichment factor for $[^{11}C]CH_3I$ estimated using the lower case of the experimentally estimated cross section (2.7×10^{-48} cm^4 s: see Eq. (10)). Parameters were beam-waist radius = 0.375 mm, optical cell radius = 0.75 mm, enrichment time = 20 min, pump-pulse duration = 10 ns. This calculation does not consider material loss by the decay of ^{11}C.

To evaluate the reliability of our method, we compared the number of ions estimated from the signal intensity per pulse with that estimated from the two-photon cross section obtained using the rate equation. We calculated the number of ions detected per pulse by our TOF system to be approximately 68 using the single-ion signal height (23 mV) from our MCP detector, considering the permeation ratio of the grid in our TOF system of 0.73 and the MCP open-area ratio [42] of 0.6. From the rate equation, we obtained the ion yield of 9–900 (Appendix A) using the effective reaction volume (Appendix B) and the effective duration (Appendix C). This range includes the result (approximately 68) from the TOF signals. Thus, the result for the ion yield is likely to prove acceptable to estimate two-photon-excitation cross sections.

In addition, we obtained the cross section for a single-photon excitation to state A and measured the ion yields for the probe-only and pump–probe modes. For these measurements, we used 266-nm pump pulses and 370-nm probe pulses with the same (80 ns) delay time between the pump and probe. The reduction ratios of the fragment and parent ions are shown in Fig. 9. We calculated the reduction ratio of the parent ion to be 0.80 ± 0.02 and the resulting excitation cross section to be $1.2 \pm 0.1 \times 10^{-19}$ cm^{-2}. Rattigan et al. [43] reported an absorption cross section for state A to be 9×10^{-19} cm^{-2}, which is about an order of magnitude larger than our result. This discrepancy is not surprising because the single-photon absorption cross section will include the effects of Raman scattering and absorption by fragment excited states, but Rattigan et al. did not include the error associated with their result. Another reason for this discrepancy might be related to the difference in sample environment within the reaction volume. Our material was exposed to an electric field for ion extraction. Considering the errors in the cross section (which are discussed in the next section) and the effects of the different environments, we consider this discrepancy to be reasonable.

From the lower case of the estimated two-photon cross section [$(4.1-1.4 = 2.7) \times 10^{-48}$ cm^4 s], we calculated the enrichment factors for $[^{11}C]CH_3I$ [Eq.(10), see Fig. 10] as a function of both pump-pulse energy and repetition rate. For this calculation, we assumed the FC factor to be 0.24, which was calculated from the R 6*p* $4;3^1_0$ transition MPI [44] and the relevant origin-band excitation signal instead of the R 6*s* $3;3^0_1$ transition. We selected this transition because this MPI scheme is unlikely to suffer from autoionization [45], and the peak MPI signal for this transition does not overlap other resonance peaks. In addition, we assumed a beam-waist radius for an enrichment of 0.375 mm, an optical-cell radius (a capillary-like cell) of 0.75 mm, and an enrichment time of 20 min, which is the half life of ^{11}C. The pulse duration was considered to be 10 ns. For pulse energy and repetition rate, we used the specifications of typical commercial dye laser systems. The results shown in Fig. 10 indicate that a high-performance laser system with a pulse power of 20 mJ and a repetition rate of 200 Hz is capable of enriching carbon-substituted methyl iodide by approximately 1700-fold. In this case, the SA of the present methyl iodide agent would be increased to the theoretically required level.

5. Discussion

We measured the two-photon-excitation cross section of the R 6*s* 3;0–0 band of CH_3I based on our pump–probe MPI experiment. From the cross section obtained for the transition from the ground state to the R 6*s* 3;0–0 state, we calculated the enrichment factor achieved by laser separation via the hot band transition. Based on the dissociation efficiency and assuming high-performance lasers are used, we find that laser separation based on the hot band transition would be practical to enrich $[^{11}C]CH_3I$ up to theoretically required SA levels. Thus, the laser separation technique seems promising for the synthesis of ^{11}C-labeld compounds use with PET radiopharmaceuticals.

However, our estimate of the high SA attainable by the proposed method includes limits to precision that result from several assumptions and experimental ambiguities. Three sources of error are included in the estimate of the cross section: (1) the misalignment of the two laser axes; (2) the thermal velocity of molecules; and (3) the effect of condensed gas (vapor).

The effect of misaligning laser beams on two-photon absorption processes has been studied by Swofford and McClain [46], who showed that a 12% signal loss occurs for a misalignment of half the radius of a Gaussian beam. In the present study, we assumed a maximum misalignment of half the radius of the laser-beam waist. If this maximum misalignment proved real, the reduction ratio obtained would be reduced by 12%; in other words, the actual cross section would increased by 13%.

The thermal velocity of the sample molecules affects the measurements because the molecules travel at this velocity during the pump–probe delay time. At room temperature, the CH_3I molecule has a root-mean square speed of 230 m/s, and hence can travel approximately 0.02 mm during the pump–probe delay time, which

is less than the diameter of the effective volume. Thus, this effect does not significantly affect the estimate of the two-photon cross section. However, by the 300 K Maxwell–Boltzmann velocity distribution, we calculated that 8% of the molecules in the reaction volume exchange with outside molecules during the pump–probe delay time. Incorporating these exchanged molecules in our calculation results in a maximum 9% increase in the two-photon cross section. From previous discussions, the two-photon cross section of the ground state transition might increase to a maximum of 21%. Such increases in the two-photon cross section would lead to an increase in the enrichment factor.

After dissociation of CH_3I in the gas phase, neutral fragments (methyl radicals and excited iodide) dissociated from the excited state can react with other molecules, which leads to a reduction in the enrichment factor. To suppress this effect, we plan to use oxygen gas in forthcoming studies as a radical scavenger [47,48]. In this scheme, oxygen gas would be mixed in with $[^{11}C]CH_3I$ vapor. In addition, in the gas phase, the excitation energy of the Rydberg state is pressure-broadened by molecular collisions, which also decreases the enrichment factor. Furthermore, experiments with additional nitrogen gas are planned because we expected additional nitrogen gas to suppress the pressure-broadening effect [49]. In short, we have to optimize the gas pressure and the ratio of additional gas components. A full discussion of the suppression effects will be part of a future presentation—the next step at this point is to study the dissociation of condensed CH_3I vapor in an optical cell.

Concerning the measurement of the cross section again, the disadvantages of our present method are the possible contribution of the velocity distribution of the target molecule and the sensitivity of the method to the alignment of the pump and probe laser beams. However, the apparatus required for the proposed method is simple and the accuracy obtained is sufficient to estimate the enrichment factor. Moreover, the proposed method is also valid for nonfluorescent molecular species other than methyl iodide, provided that the molecule dissociates faster than the excitation rate and that its fragments cannot be ionized by the probe pulse. By monitoring the spatial distributions of pump and probe beams to ensure proper alignment and optimizing the conditions that determine the thermal velocity contribution of the target molecules, we should be able to increase the current accuracy of the proposed method to estimate two-photon-excitation cross sections.

6. Conclusion

Our pump–probe MPI experiment demonstrated that the two-photon-excitation cross section of the R 6*s* 3;0–0 of CH_3I contributed to increase to the specific activity (SA). The enrichment factor could be achieved by a factor of 1700 with laser separation via the hot band transition (R 6*s* $3;3_1^0$) using the presently available high-performance laser system. However, effects of collision and/or fragment reactions caused by the dissociation of the molecule in the gas phase can be factors that limit its performance. Therefore, further study is required in PET radiosynthesis environment.

Acknowledgments

We are indebted to Iwao Kanno of the National Institute of Radiological Sciences (NIRS), Japan, for his encouragement. Also, we would like to thank Jeff Kershaw of the NIRS for his comments concerning our manuscript. We would like to thank Enago (www.enago.jp) for the English language review. This study was partially supported by a consignment expense for Molecular Imaging Program on "Research Base for PET Diagnosis" from the Ministry of Education, Culture, Sports, Science and Technology (MEXT), Japan.

Appendix A. Rate equation

To consider the kinetics of a multiphoton process (via excitation) of a molecule, the rate equations of the process [17,50,51] are used. The rate equations for the (2 + 1) REMPI process are

$$\frac{dX}{dt} = \sigma_{ex}^{(2)} I^2 (A - X), \tag{A.1}$$

$$\frac{dA}{dt} = \sigma_{ex}^{(2)} I^2 (X - A) - \left\{ \frac{1}{T} + \left(\sigma_i^{(ex)} I \right) \right\} A, \tag{A.2}$$

$$\frac{dC}{dt} = \sigma_i^{(ex)} I A, \tag{A.3}$$

where X, A and C are the populations of the ground state, excited state and ionization continuum, respectively; $\sigma_i^{(ex)}$ is the ionization cross section for the transition to the excited state; and T is the excited state lifetime (dissociation). For the study reported herein, the peak photon density (I) was 3.45×10^{27} ($cm^{-2}\ s^{-1}$) and the lifetime of the excited state (6*s* Rydberg [3]) is considered to be 10^{-13}–10^{-12} s [52]. The two-photon cross sections of the excitation ($\sigma_{ex}^{(2)}$) and subsequent ionization are assumed to be 10^{-49}–10^{-48} (cm^4 s) and 10^{-19}–10^{-18} (cm^2), respectively, which we obtained by employing typical values for REMPI dynamics [53]. The parameters calculated from these inputs satisfy the condition $\sigma_{ex}^{(2)} I^2 << \sigma_i^{(ex)} I << 1/T$. In the case, the rate equations are resolved approximately as follows:

$$X(\Delta t) = \mathrm{X}(0) - \sigma_{ex}^{(2)} I^2 \Delta t. \tag{A.4}$$

We see that the dissociation rate $[-\Delta X/\Delta t]$ of the molecule corresponds to the excitation rate ($\sigma_{ex}^{(2)} I^2$). Moreover, under these conditions, the population of the ionization continuum is approximated as follows:

$$C(\Delta t) = \sigma_{ex}^{(2)} \sigma_i^{(ex)} I^3 T \Delta t. \tag{A.5}$$

Therefore, the ion yield (Q) per pulse from the reaction volume (V) of the number density (ρ) is given by

$$Q = V \rho \sigma_{ex}^{(2)} \sigma_i^{(ex)} I^3 T \Delta t. \tag{A.6}$$

For simplicity, this derivation has been based on a laser beam with a rectangular spatial distribution.

Appendix B. Spatial Gaussian model

We presume that the dilute target gas with number density (ρ) is irradiated by a focused laser pulse. The number Q of ions or excited molecules produced by the nth-order multiphoton process is calculated [54] from the peak photon density I, the effective reaction volume $V^{(n)}$, and the effective pulse duration $\tau^{(n)}$:

$$Q = \rho \sigma^{(n)} I^n V^{(n)} \tau^{(n)}. \tag{B.1}$$

Here we follow Gandhi and Bernstein [54] to introduce our approach. The effective reaction volume is described by

$$V^{(n)} = \int P_s^n(r,z) \mathrm{d}V = \int_{-\infty}^{\infty} \int_0^{\infty} P_s^n(r,z) 2\pi r \, dr \, dz, \tag{B.2}$$

where P_s is the spatial distribution function, z is the beam direction, and r is the radial distance from the beam axis. We assume that the transverse laser-intensity distribution is Gaussian. The spatial distribution function can be written as [55,56]

$$P_s(r,z) = \frac{1}{1+(az)^2} \cdot \exp\left(-\frac{r^2}{w^2\left[1+(az)^2\right]}\right), a = \frac{\lambda}{2\pi w^2}, \quad \text{(B.3)}$$

where w is the beam waist-radius, λ is the laser wavelength.

In the present study, the integral z range in Eq. (B.2) should be limited to within the diameter (L_z = 14.5 mm) of the open area of the MCP ion detector. In this range, we can assume that the Gaussian radius ($1/e$) corresponds to the beam waist radius w created by a 300-mm focal length lens and is approximately constant at the z-position within the sample cell. Therefore, Eq. (B.2) can be rewritten as

$$V^{(n)} = L_z \int_0^\infty P_s^n(r,0) 2\pi r\, dr. \quad \text{(B.4)}$$

For simplification, we define

$$P(r/w) = \exp\left[-\left(\frac{r}{w}\right)^2\right], \quad \text{(B.5)}$$

which we use to rewrite Eq. (B.4) as

$$V^{(n)} = L_z \int_0^\infty P^n\left(\frac{r}{w}\right) 2\pi r\, dr \quad \text{(B.6)}$$

Therefore, Eq. (B.1) takes the form

$$Q = \rho\sigma^{(n)} I^n \int P^n\left(\frac{r}{w}\right) 2\pi r\, dr\; L_z \tau^{(n)}. \quad \text{(B.7)}$$

Under these conditions, the effective reaction volume and the effective reaction area A_n introduced by Gandhi and Bernstein [54] as

$$\int P_s^n(r,z)\, dV = V_n = A_n L_n \quad \text{(B.8)}$$

become real. The dependence of the reaction volume on photon multiplicity is given as

$$V_n = \frac{V}{n}, \left(\text{or } A_n = \frac{S}{n}\right), \quad \text{(B.9)}$$

where S is the cross-sectional area of the laser beam at the beam waist:

$$S = \pi w^2. \quad \text{(B.10)}$$

Appendix C. Temporal Gaussian model

We also assume a Gaussian temporal distribution for the laser pulse. Therefore, referring to the literature [57], the effective pulse duration from Appendix B is related to the FWHM of the Gaussian pulse by

$$\tau^{(n)} = \frac{\Delta t}{\sqrt{n}} \quad \text{(C.1)}$$

References

[1] G.B. Saha, Basics of PET Imaging, Springer, New York, 2004. p. 106.
[2] P.H. Elsinga, Methods 27 (2002) 208–217.
[3] M. Allard, E. Fouquet, D. James, M. Szlosek-Pinaud, Curr. Med. Chem. 15 (2008) 235–277.
[4] C. Crouzel, B. Langstrom, V.W. Pike, H.H. Coenen, Appl. Radiat. Isotopes 38 (1987) 601–603.
[5] V. Gomez-Vallejo, J. Flop, Appl. Radiat. Isotopes 67 (2009) 111–114.
[6] M.-R. Zhang, K. Suzuki, Appl. Radiat. Isotopes 62 (2005) 447–450.
[7] R. Iwata, T. Ido, A. Ujiie, T. Takahashi, K. Ishiwata, K. Hatano, M. Sugahara, Appl. Radiat. Isotopes 39 (1988) 1–7.
[8] J. Yui, A. Hatori, K. Kawamura, K. Yanamoto, T. Yamasaki, M. Ogawa, Y. Yoshida, K. Kumata, M. Fujinaga, N. Nengaki, T. Fukumura, K. Suzuki, M.-R. Zhang, NeuroImage 54 (2011) 123–130.
[9] J. Noguchi, M.-R. Zhang, K. Yanamoto, R. Nakao, K. Suzuki, Nucl. Med. Biol. 35 (2008) 19–27.
[10] J. Noguchi, K. Suzuki, Nucl. Med. Biol. 30 (2003) 335–343.
[11] V.S. Letokhov, Ann. Rev. Phys. Chem. 28 (1977) 133–159.
[12] V.S. Letokhov, Nature 277 (1979) 605–610.
[13] D.H. Parker, R. Pandolfi, P.R. Stannard, M.A. El-Sayed, Chem. Phys. 45 (1980) 27–37.
[14] A. Wakai, K. Tsuchida, T. Fukumura, K. Suzuki, Chem. Phys. Lett. 516 (2011) 23–28.
[15] S. Felps, P. Hochmann, P. Brint, S.P. McGlynn, J. Mol. Spectrosc. 59 (1976) 355–379.
[16] W.S. Felps, J.D. Scott, S.P. McGlynn, J. Chem. Phys. 104 (1996) 419–429.
[17] P.M. Johnson, C.E. Otis, Ann. Rev. Phys. Chem. 32 (1981) 139–157.
[18] M. Sheik-Bahae, A.A. Said, T. Wei, D.J. Hagan, E.W. Van Stryland, IEEE J. Quantum Electron. 26 (1990) 760–769.
[19] C. Wang, L. Liu, W. Ma, Z. Zhou, G. Wang, Z. Xu, Optik 116 (2005) 75–79.
[20] C. Xu, W.W. Webb, J. Opt. Am. B 13 (1996) 481–491.
[21] M.V. Ashikhmin, Yu.E. Belyaev, A.V. Dem'yanenko, E.A. Ryabov, V.S. Letokhov, Chem. Phys. Lett. 227 (1994) 343–348.
[22] J.L. Knee, L.R. Khundkar, A.H. Zewail, J. Chem. Phys. 83 (1985) 1996–1998.
[23] L.R. Khundkar, A.H. Zewail, Annu. Rev. Phys. Chem. 41 (1990) 15–60.
[24] Y. Wang, H. Shen, L. Hua, C. Hu, B. Zhang, Opt. Express 17 (2009) 10506–10513.
[25] D.H. Parker, M.A. El-Sayed, Chem. Phys. 42 (1979) 379–387.
[26] L. Poth, Q. Zhong, J.V. Ford, A.W. Castleman Jr., J. Chem. Phys. 109 (1998) 4791–4797.
[27] A.P. Baranavski, J.C. Owrutsky, J. Chem. Phys. 108 (1998) 3445–3452.
[28] D. Zhong, A.H. Zewail, J. Phys. Chem. A 102 (1998) 4031–4058.
[29] G. Gizinger, M.E. Corrales, V. Loriot, G.A. Amaral, R. de Nalda, L. Bañares, J. Chem. Phys. 132 (2010) 234313.
[30] P. Brewer, P. Das, G. Ondrey, R. Bersohn, J. Chem. Phys. 79 (1983) 720–723.
[31] H. Kojima, T. Fukumi, S. Nakajima, Y. Maruyama, K. Kosaka, Chem. Phys. Lett. 95 (1983) 614–617.
[32] J.H. Clark, Y. Haas, P.L. Houston, C.B. Moore, Chem. Phys. Lett. 35 (1975) 82–85.
[33] R.V. Ambartzumian, N.P. Furzikov, Yu.A. Gorokhov, V.S. Letokhov, G.N. Makarov, A.A. Puretzky, Opt. Commun. 18 (1976) 517–521.
[34] G. Hancock, J.D. Campbell, K.H. Welge, Opt. Commun. 16 (1976) 177–181.
[35] A. Fahr, A.K. Nayak, M.J. Kurylo, Chem. Phys. 197 (1995) 195–203.
[36] J. Tellinghuisen, Adv. Chem. Phys. 60 (1985) 299–368.
[37] H. Guo, A.H. Zewail, Can. J. 72 (1994) 947.
[38] Y.-K. Choi, Y.-M. Koo, K.-W. Jung, J. Photochem. Photobiol., A 127 (1999) 1–5.
[39] Y. Jiang, M.R. Giorigi-Arnazzi, R.B. Bernstein, Chem. Phys. 106 (1986) 171–178.
[40] A.B. Alekseyev, H.-P. Lebermann, R.J. Buenker, J. Chem. Phys. 134 (2011) 044303. They did not study the 6s Rydberg [3] state of CH_3I. We decided to use excited iodine by analogy of R 6s [4] and [2] in Fig. 2 in the their report.
[41] D.W. Chandler, J.W. Thoman Jr., Chem. Phys. Lett. 156 (1989) 151–158.
[42] S. Matsuura, S. Umebayashi, C. Okuyama, K. Oba, IEEE Trans. Nucl. Sci. NS-32 (1985) 350–354.
[43] O.V. Rattigan, E.E. Shallcross, R.A. Cox, J. Chem, Soc. Faraday Trans. 93 (1997) 2839–2846.
[44] H. Guo, A.H. Zewail, Can. J. Chem. 72 (1994) 947–957.
[45] B. Urban, V.E. Bondybey, J. Chem. Phys. 116 (2002) 4938–4947.
[46] R.L. Swofford, W.M. McClain, Chem. Phys. Lett. 34 (1975) 455–460.
[47] J. Heicklen, H.S. Johnston, J. Am. Chem. Soc. 84 (1962) 4030–4039.
[48] J. Farren, J.R. Gilbert, J.W. Linnett, I.A. Read, J. Chem. Soc. Trans. Faraday 60 (1964) 740–750.
[49] U. Asaf, K. Rupnik, G. Reisfeld, S.P. McGlynn, J. Chem. Phys. 99 (1993) 2560–2566.
[50] D.S. Zakheim, P.H. Johnson, Chem. Phys. 46 (1980) 263–272.
[51] B. Zheng, M. Lin, B. Zhang, W. Chen, Opt. Commun. 73 (1989) 208–212.
[52] D.J. Campbell, L.D. Ziegler, Chem. Phys. Lett. 201 (1993) 159–165.
[53] D.H. Parker, J.O. Berg, M.A. El-Sayed, in: A.H. Zewail (Ed.), Advances in Laser Chemistry (Springer series in Chemical Physics 3), Springer, Berlin, Heidelberg, New York, 1978, pp. 320–335.
[54] S.R. Gandhi, R.B. Bernstein, Chem. Phys. 105 (1986) 423–434.
[55] M.V. Ammosov, N.B. Delone, M.Yu. Ivanov, Adv. Atom., Mol., Opt. Phys. 29 (1992) 33–110.
[56] A. L'Huillier, L.A. Lompre, G. Mainfray, C. Manus, J. Phys. B: Atom. Mol. Opt. Phys. 16 (1983) 1363–1381.
[57] D. Normand, J. Morellec, J. Phys. B: Atom. Mol. Phys. 13 (1980) 1551–1561.

Original Paper

Cerebrovascular Diseases

Cerebrovasc Dis
DOI: 10.1159/000332034

Received: February 24, 2011
Accepted: August 15, 2011
Published online: ■■■

Safety of Low-Frequency Transcranial Ultrasound in Permanent Middle Cerebral Artery Occlusion in Spontaneously Hypertensive Rats

Zuojun Wang[a, d] Takahiro Fukuda[b] Takashi Azuma[c] Hiroshi Furuhata[a]

[a]Medical Engineering Laboratory, [b]Division of Neuropathology, Research Center for Medical Sciences, Jikei University School of Medicine, and [c]Department of Biomedical Research, Faculty of Engineering, University of Tokyo, Tokyo, Japan; [d]Department of Ultrasonic Medicine, Tangdu Hospital, Fourth Military Medical University, Xi'an, China

Key Words

Acute stroke · Cerebral ischemia · Experimental stroke research · Intracranial hemorrhage · Hypertension · Thrombolysis · Ultrasound

Abstract

Background: Some studies suggest that low-frequency transcranial ultrasound (LFTUS) can enhance thrombolysis, but other studies suggest that it may have adverse effects on intracranial tissues. We previously reported that LFTUS with appropriate parameters was effective and safe in a normotensive rat model of thromboembolic middle cerebral artery occlusion (MCAO) stroke. The goal of this study was to test the safety of this strategy in a spontaneously hypertensive rat (SHR) model of permanent MCAO. ***Methods:*** Right MCAO was achieved in male SHRs using intraluminal nylon sutures. Rats exhibiting left hemiparesis were randomly assigned to one of four different groups: (1) normal saline (NS) group (n = 8), intravenous administration of NS as placebo at 3 h after MCAO; (2) NS+LFTUS group (n = 10), NS administration with simultaneous application of LFTUS (480.4 kHz, continuous wave, at an intensity of 0.3 W/cm^2) for 1 h; (3) tissue plasminogen activator (tPA) group (n = 11), intravenous administration of alteplase (10 mg/kg body weight) over 1 h instead of NS; or (4) tPA+LFTUS group (n = 11), tPA administration and application of LFTUS. Twenty-four hours after treatment, neurological change was evaluated, and brains were removed and examined histologically. ***Results:*** There was no significant difference ($p > 0.09$) when comparing changes in neurologic status and body weight, infarct ratio, edema ratio, or hemorrhagic transformation among the four groups. ***Conclusions:*** Our findings suggest that sonothrombolytic treatment with LFTUS with appropriate parameters is safe when used for the treatment of ischemic stroke in hypertensive rats under the undesired permanent MCAO condition.

Introduction

The thrombolytic efficacy of transcranial ultrasound in the treatment of acute ischemic stroke (AIS) [1–6] has attracted a great deal of attention among stroke investigators. Indeed, low-frequency ultrasound enhances the thrombolytic effect of other modalities [7–10] and has good skull penetration [11–13]. However, the TRUMBI trial demonstrated that low-frequency transcranial ultrasound (LFTUS) is associated with a very high rate of symptomatic intracranial hemorrhages in patients with AIS [14]. Studies performed to investigate the reasons for these complications [15–18] suggest that hemorrhage

KARGER

Fax +41 61 306 12 34
E-Mail karger@karger.ch
www.karger.com

1015–9770/11/0000–0000$38.00/0
Accessible online at:
www.karger.com/ced

Zuojun Wang, MD
Medical Engineering Laboratory
Jikei University School of Medicine
3-25-8 Nishi-shinbashi, Minato-ku, Tokyo 105-8461 (Japan)
Tel. +81 3 3433 1111, ext. 2338, E-Mail wangzj@jikei.ac.jp

may be related to a variety of factors, including intensity-dependent effects in the brain [15] and disruption of the blood-brain barrier [16].

These adverse effects of LFTUS may be dependent on the specific ultrasound settings. We previously reported that 490 kHz LFTUS with appropriate parameters was safe and effective in a normotensive Wistar rat model of middle cerebral artery occlusion (MCAO) [19]. However, hypertension is present in more than half of AIS patients [20]. Therefore, the goal of the present study was to determine whether LFTUS is safe in a spontaneously hypertensive rat (SHR) model of permanent MCAO.

Methods

All animal procedures were performed under the guidance of the animal research committee (Jikei University School of Medicine, Tokyo, Japan). Forty-five male, 12-week-old SHRs (Sankyo Labo Service Corp. Inc., Tokyo, Japan) were used in this study.

The rats were anesthetized via inhalation of isoflurane in air (4.8% for induction, 2.5% for surgery, and 1–2% for treatment) during both surgical and therapeutic procedures. Rectal temperature was maintained at 37.5 ± 0.5°C during all procedures with a thermal control blanket (BWT-100; BRC Co. Ltd., Nagoya, Japan).

Surgical Procedures

MCAO was achieved in SHR using a method modified from Koizumi et al. [21]. Briefly, under a surgical microscope, the right common, internal, and external carotid arteries were identified through a cervical midline incision. The external carotid artery and the occipital artery were ligated with a 4–0 silk suture. The internal carotid artery was temporarily closed with a Sugita aneurysm clip (temporary mini-type; Mizuho Ikagaku Industries, Tokyo, Japan), and the common carotid artery was closed using a suture 3-mm proximal to the carotid bifurcation. A small incision was made in the common carotid artery 1 mm proximal to the carotid bifurcation, and a 2–0 nylon suture was inserted from the common carotid artery into the internal carotid artery. After removing the Sugita clip, the suture was advanced 17–19 mm beyond the carotid bifurcation until mild resistance was felt. This resulted in occlusion at the origin of the MCA. Then, the cervical incision was closed and anesthesia was terminated.

Neurologic Evaluation and Body Weight Measurement

On a 5-point scale [22] (0 = no apparent deficits; 1 = contralateral forelimb flexion; 2 = decreased grip of the contralateral forelimb while tail pulled; 3 = spontaneous movement in all directions and contralateral circling only if pulled by tail; 4 = spontaneous contralateral circling), neurologic evaluation was blindly performed before surgery, just before treatment (3 h after MCAO) and at 24 h after treatment. Animals showing a neurologic score of 0 before surgery and a score of 3 or 4 before treatment were included in this study. The body weights of animals were also measured with an animal scale (SL-1000; A&D Co. Ltd., Seoul, Korea) at the time points described above.

Treatment Groups

Of the 45 rats used, 1 animal had a neurologic score of 0 before treatment, and we were unable to administer drug treatment intravenously in 4 animals. Thus, these animals were excluded from further study. Study animals (n = 40) were randomly assigned to one of the following four treatment groups: (1) normal saline (NS) group (n = 8), intravenous administration of NS as placebo via the tail vein (10 ml/kg body weight; 10% as a bolus, and the remainder infused over 60 min) at 3 h after MCAO; (2) NS+LFTUS group (n = 10), NS administration and application of LFTUS; (3) tissue plasminogen activator (tPA) group (n = 11), intravenous administration of tPA [alteplase (Mitsubishi Tanabe Pharma Corp., Osaka, Japan); 1 mg/ml, 10 ml/kg body weight; 10% as a bolus, and the remainder infused over 60 min] instead of NS; and (4) tPA+LFTUS group (n = 11), alteplase administration and application of LFTUS. The potency of human tPA in rats is approximately 10% of that in humans [23], i.e. a tPA dose of 10 mg/kg body weight in rats is equivalent to a therapeutic dose of tPA that is typically used for AIS in humans (0.9 mg/kg body weight).

Ultrasound System and Method

The ultrasound system utilized in this study has been described previously [19]. Briefly, the ultrasound transducer was custom-made for animal studies, with a plane circular surface of 5 mm in diameter and a resonant frequency of 480.4 kHz. The transducer was driven by a custom-made signal generator through a power amplifier (No. 4055; NF Corp, Yokohama, Japan) and a custom-made matching box. The transducer was set on the right scalp, centered 3 mm from the midline and 1 mm posterior to the bregma, with the help of a stereotaxic instrument (IMPACT-1000B; Muromachi Kikai, Tokyo, Japan). To enable better ultrasound transmission, the respective scalp area was depilated, and a layer of ultrasound gel was applied to the scalp before applying the transducer. Ultrasound conditions included a frequency of 480.4 kHz and spatial average intensity of 0.3 W/cm^2. Under this condition, the spatial peak intensity was approximately 1.2 W/cm^2, the mechanical index (MI) was 0.28, and the thermal index for the cranial bone was 2.9. Ultrasound output was confirmed with an ultrasound power meter (UPM-DT-1; Ohmic Instruments Co., Easton, Md., USA) before and after each treatment.

The ultrasound beam inside the rat cranial cavity was studied in a preliminary experiment using the schlieren method (fig. 1a) and the hydrophone (effective diameter, 0.2 mm) method (fig. 1b).

To avoid tissue heating, LFTUS was applied intermittently as previous described [19]. Briefly, after 2 min of continuous wave, irradiation was interrupted for 30 s. This pattern of application was repeated four times during a 10-min period, after which LFTUS was not performed for 5 min to enable cooling. These 10-min cycles of LFTUS, each followed by a 5-min break, were repeated four times over a period of 60 min.

Brain Extraction

After neurologic evaluation at 24 h after treatment, rats were deeply anesthetized with an intraperitoneal injection of 100 mg/kg of pentobarbital sodium (Somnopentyl; Kyoritsu Seiyaku Corp., Tokyo, Japan) and transcardially perfused with 50 ml of heparinized saline (5 U/ml) and 50 ml of 10% buffered formalin. Then, the brain, along with the front portion of the inserted nylon suture, was carefully extracted from the cranium. Photographs of brain surfaces and the intracranial cavity were taken to record the

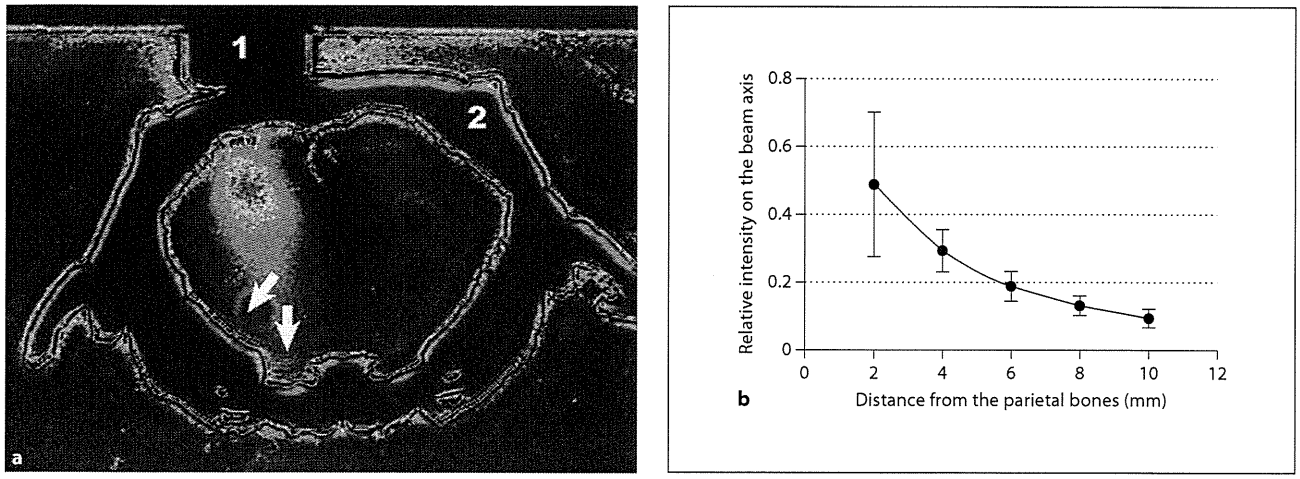

Fig. 1. a The ultrasound field inside a rat cranium observed with the schlieren method; 1 = LFTUS probe; 2 = rat cranium. The LFTUS probe was set on the parietal side of the rat cranium. The arrows indicate the formation of a standing wave as a striped pattern near the opposite side of the cranium. **b** The relative intensity of the LFTUS on the beam axis after its penetration through the parietal side of the rat cranium (n = 8).

position of the inserted suture and to document any visible abnormality on the brain and in the cranial cavity, including the potential presence of subarachnoid hemorrhage.

Cerebral Infarct and Edema Ratio

Each brain was cut into 2-mm-thick coronal sections. Six coronal sections (positioned 2–14 mm from the front pole) were obtained from each brain. Then, 3-μm thinly sliced specimens were prepared and stained with hematoxylin and eosin. Stained specimens were scanned with a flathead scanner (ES-8500; Seiko Epson Corp., Nagano, Japan) at a resolution of 3,200 dots per inch. The scanned images were analyzed with Photoshop image processing software. The infarct area in each section was measured as follows: (1) the infarct region was carefully selected in Photoshop with the lasso tool; (2) the pixel number of the selected region was determined in the histogram panel in Photoshop; and (3) the infarct area was determined by dividing the pixel number by the pixel density ($3,200 \times 3,200 = 10,240,000/\text{inch}^2 \approx 15,872/\text{mm}^2$). The infarct volume (IV) was calculated by summing the corresponding areas over all six sections and then multiplying the sum by the slice thickness (2 mm). The left hemisphere volume (LV) and the right hemisphere volume (RV) were determined in a similar manner. The edema ratio (ER) was calculated using the formula: $ER = (RV - LV)/LV \times 100\%$, and the edema-corrected infarct ratio (IR) was calculated using a formula similar to that proposed by Swanson et al. [24]: $IR = (LV - (RV - IV))/LV \times 100\%$.

Measurement of Intracerebral Hemorrhage

LFTUS has different field characteristics in the intracranial cavity (fig. 1), with the part near the parietal bone having stronger intensity and the part near the opposite cranium having a standing wave. Thus, intracerebral hemorrhage was examined at three different levels (i.e. 'near', 'middle', and 'far'; each occupying one third of the distance from the parietal side to the base side of the brain).

Hemorrhage was classified as macroscopic hemorrhage or microscopic hemorrhage. Macroscopic hemorrhage was defined as blood evident to the unaided eye on the hematoxylin and eosin-stained coronal sections and was graded according to its cross-sectional area (1: <0.8; 2: 0.8–3.1; 3: 3.1–7.1; 4: >7.1 mm^2) [25]. Microscopic hemorrhage was defined as a cluster of red blood cells outside of the lumen of blood vessels that could only be identified under microscopy [26]. Area of microscopic hemorrhage was measured with digital micrographs (4,116 × 3,072) taken with a ×20 objective lens of a Nikon biomicroscope (Eclipse 800-i) and summed for each level as well as for the whole hemisphere.

Statistical Analysis

Qualitative data (including neurologic score, mortality rate, subarachnoid hemorrhage rate, and macroscopic cerebral hemorrhage rate) were analyzed statistically using Fisher's exact test. Quantitative data (including body weight, IR, ER, and microscopic hemorrhage area) were presented as means ± SD and compared using one-way ANOVA. Differences with $p < 0.05$ were considered statistically significant.

Results

Mortality, Neurologic Score, and Body Weight Changes

One animal from the NS group died within 24 h of treatment. Neither subarachnoid hemorrhage nor significant intracerebral hemorrhage was found, but the ER (28.4%) was relatively high in this animal, which might

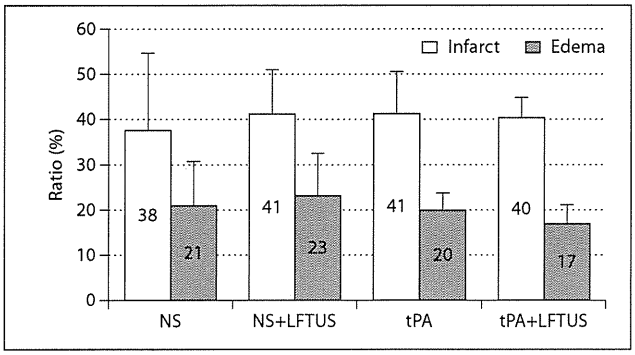

Fig. 2. Comparison of IR and ER. There was no significant difference among the four treatment groups in either of these indices.

have accounted for the mechanism of death. There was no significant difference in mortality rate ($p = 0.26$) among the four study groups. Nearly all animals had a neurologic score of 4 before treatment and a neurologic score of 3 at 24 h after treatment. There was no significant difference in neurologic score or change in body weight when comparing the four study groups.

Suture Position and Subarachnoid Hemorrhage

The inserted intraluminal suture was entered into the right anterior cerebral artery in all animals. Subarachnoid hemorrhage occurred in only one animal in the tPA group. There was no significant difference in the incidence of subarachnoid hemorrhage ($p = 0.45$) when comparing the four study groups.

Infarct Volume and Brain Edema

The IR was approximately 40%, and the ER was approximately 20% in all four study groups (fig. 2). There was no significant difference in IR ($p = 0.9$) or ER ($p = 0.25$) when comparing the four study groups.

Intracerebral Hemorrhage

Macroscopic hemorrhage occurred in 2 animals (1 in the NS+LFTUS group and 1 in the tPA group), both of which were in the 'middle' level (fig. 3) and were scored as grade 1 (i.e. area less than 0.8 mm^2). There was no significant difference in the macroscopic hemorrhage rate when comparing the four study groups (table 1). Microscopic hemorrhage measurements are also shown in the table. There was no significant difference in microscopic hemorrhage area when comparing the four study groups.

Discussion

This study found no significant difference among the four groups in any of the examined indices, including change in neurologic score, IR, ER, and hemorrhagic transformation. These results suggest that LFTUS is a safe therapeutic strategy in a hypertensive animal model of permanent occlusion. It should be noted that because this study explored the safety of LFTUS under the undesired permanent MCAO condition by using an indissoluble intraluminal suture to occlude the middle cerebral artery, it was unable to characterize any potential beneficial effects of ultrasound-mediated enhancement of thrombolysis, such as a decrease of infarct size [9] or alleviation of neurological score [19].

More than half of AIS patients have a history of hypertension [20], and hypertension is independently associated with poor outcome [27]. Therefore, many experimental studies of AIS, including those characterizing the therapeutic efficacy of tPA, utilize an SHR model of temporary MCAO [28]. However, nonrecanalization in response to clinical tPA treatment is not uncommon. Further, the TRUMBI trials showed that many symptomatic intracranial hemorrhages occurred in patients treated with LFTUS, who also had a low recanalization rate [14]. Therefore, the present study utilized an SHR model of permanent MCAO to test the safety of LFTUS.

The bleeding risk of thrombolytic treatment is closely related to (delayed) recanalization [25]. In Koizumi's permanent MCAO model, the thrombolytic effect of tPA is limited to the freshly formed thrombus around the suture in the occluded vessels, and the intraluminal suture cannot be dissolved to result in recanalization. Therefore, this model cannot evaluate the bleeding risk associated with (delayed) thrombolytic recanalization. However, one of the most important potential risks of the combined treatment of LFTUS with or without tPA may be its direct adverse effect on the disease or even healthy cerebral vessels [14]. In this context, use of Koizumi's MCAO model may be more appropriate than other models for the purposes of separating such direct adverse effects from those caused indirectly by thrombolytic recanalization.

This study demonstrated that sonothrombolysis with LFTUS was safe when used as late as 3 h after permanent MCAO in SHR. We propose that the safety of LFTUS is related to several different factors. First, LFTUS utilized in the present study had a low MI. In fact, with a continuous wave and a spatial average intensity of 0.3 W/cm^2, the corresponding spatial peak intensity was only about 1.2 W/cm^2, and the MI was only about 0.28. Thus, the MI

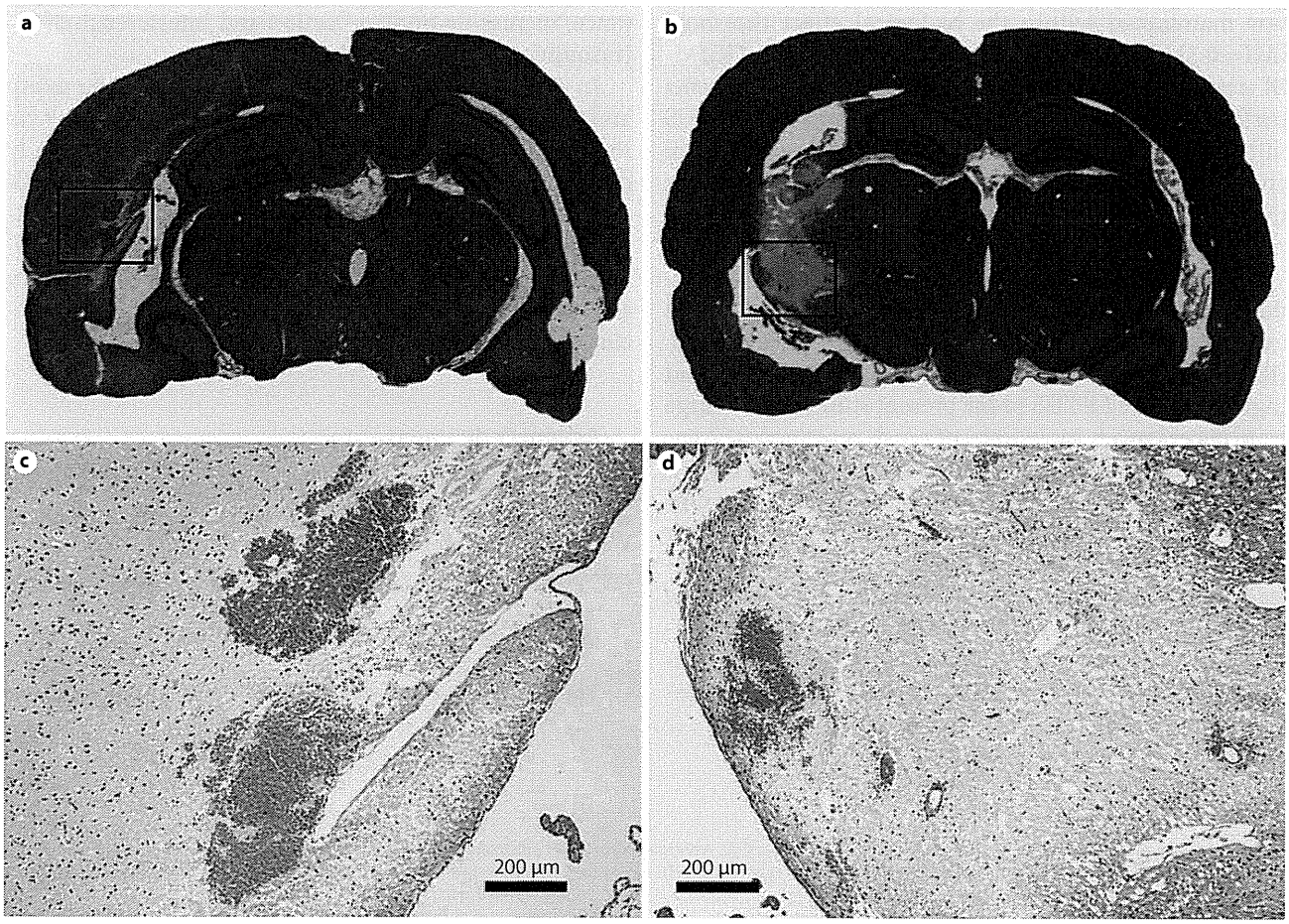

Fig. 3. Photographs of hematoxylin and eosin-stained rat brains of the 2 cases of macroscopic intracranial hemorrhages occurring in the tPA group (**a**) and the NS+LFTUS group (**b**). **c**, **d** Photomicrographs of the enclosed areas in **a** and **b**, respectively. Both macroscopic intracranial hemorrhages located in the 'middle' level of brain suggest little relationship with the applied TUS, of which intensity was stronger at the 'near' level and standing waves mainly occurred at the 'far' level.

Table 1. Intracerebral hemorrhages

Groups	Macroscopic hemorrhage rate (%)				Microscopic hemorrhage area ($\times 10^2$ μm^2)			
	near	middle	far	sum	near	middle	far	sum
NS (n = 8)	0	0	0	0	35 ± 78	103 ± 76	81 ± 81	219 ± 188
NS+LFTUS (n = 10)	0	10	0	10	111 ± 192	148 ± 276	186 ± 187	445 ± 383
tPA (n = 11)	0	9	0	9	160 ± 361	116 ± 378	116 ± 143	392 ± 578
tPA+LFTUS (n = 11)	0	0	0	0	160 ± 179	87 ± 235	175 ± 247	368 ± 356
p value	1.00	0.84	1.00	0.84	0.73	0.75	0.61	0.65

was maintained within the biological effect threshold (MI = 0.5) [29], much lower than that used in the TRUMBI trial (MI = 1.2) and that used in animal experiments performed by Schneider et al. [15]. Second, the LFTUS utilized in the present study had a well-controlled beam aperture (only about 20 mm^2). The transducers used in the TRUMBI trial [14] had a total area of about 2,830 mm^2, which is about 18-fold of that (≈150 mm^2) of a conventional clinical transcranial Doppler ultrasound transducer. In addition, the transducers used in the animal experiments by Schneider et al. [15] and by Reuter et al. [18] were also relatively large (350 mm^2, about 17.5-fold higher than the LFTUS in the present study). These large transducers result in delivery of much more acoustic energy into the intracranial cavity and increase the formation of dangerous standing waves near the opposite cranium [10, 30]. Third, the frequency (≈500 kHz) of our LFTUS was higher than those used in other LFTUS studies (e.g. 300 kHz in the TRUMBI trial and 20 kHz in the study by Schneider et al. [15]). An excessively low frequency may increase the MI at the same spatial peak intensity [29] and result in excessively long penetration distance, increasing multireflection and interference of ultrasound waves within the cranium [10].

In conclusion, we previously demonstrated the safety and efficacy of our LFTUS in a normotensive Wistar rat model of thromboembolic MCAO. The present study demonstrated the safety of this strategy in an SHR model of permanent MCAO. However, because serious intracranial hemorrhages may occur more easily when recanalization occurs, further study of the safety of LFTUS in a clinically relevant hypertensive model of temporary occlusion model is necessary.

Acknowledgement

This work was supported by grant H21-008 for research on advanced technology from the Ministry of Health, Labor, and Welfare of Japan.

Disclosure Statement

The authors declare that they have no conflicts of interest.

References

1 Alexandrov AV, Molina CA, Grotta JC, Garami Z, Ford SR, Alvarez-Sabin J, Montaner J, Saqqur M, Demchuk AM, Moye LA, Hill MD, Wojner AW, CLOTBUST Investigators: Ultrasound-enhanced systemic thrombolysis for acute ischemic stroke. N Engl J Med 2004;351:2170–2178.

2 Cintas P, Le Traon AP, Larrue V: High rate of recanalization of middle cerebral artery occlusion during 2-MHz transcranial color-coded Doppler continuous monitoring without thrombolytic drug. Stroke 2002;33:626–628.

3 Holscher T, Raman R, Ernström K, Parrish J, Le DT, Lyden PD, Mattrey RF: In vitro sonothrombolysis with duplex ultrasound: first results using a simplified model. Cerebrovasc Dis 2009;28:365–370.

4 Meairs S, Culp W: Microbubbles for thrombolysis of acute ischemic stroke. Cerebrovasc Dis 2009;27(suppl 2):55–65.

5 Molina CA, Ribo M, Rubiera M, Montaner J, Santamarina E, Delgado-Mederos R, Arenillas JF, Huertas R, Purroy F, Delgado P, Alvarez-Sabin J: Microbubble administration accelerates clot lysis during continuous 2-MHz ultrasound monitoring in stroke patients treated with intravenous tissue plasminogen activator. Stroke 2006;37:425–429.

6 Molina CA, Alvarez-Sabín J: Recanalization and reperfusion therapies for acute ischemic stroke. Cerebrovasc Dis 2009;27(suppl 1):162–167.

7 Nedelmann M, Eicke BM, Lierke EG, Heimann A, Kempski O, Hopf HC: Low-frequency ultrasound induces nonenzymatic thrombolysis in vitro. J Ultrasound Med 2002;21:649–656.

8 Suchkova V, Carstensen EL, Francis CW: Ultrasound enhancement of fibrinolysis at frequencies of 27 to 100 kHz. Ultrasound Med Biol 2002;28:377–382.

9 Daffertshofer M, Huang Z, Fatar M, Popolo M, Schroeck H, Kuschinsky W, Moskowitz MA, Hennerici MG: Efficacy of sonothrombolysis in a rat model of embolic ischemic stroke. Neurosci Lett 2004;361:115–119.

10 Wang Z, Moehring MA, Voie AH, Furuhata H: In vitro evaluation of dual mode ultrasonic thrombolysis method for transcranial application with an occlusive thrombosis model. Ultrasound Med Biol 2008;34:96–102.

11 Akiyama M, Ishibashi T, Yamada T, Furuhata H: Low-frequency ultrasound penetrates the cranium and enhances thrombolysis in vitro. Neurosurgery 1998;43:828–832.

12 Behrens S, Daffertshofer M, Spiegel D, Hennerici M: Low-frequency, low intensity ultrasound accelerates thrombolysis through the skull. Ultrasound Med Biol 1999;25:269–273.

13 Behrens S, Spengos K, Daffertshofer M, Schroeck H, Dempfle CE, Hennerici M: Transcranial ultrasound-improved thrombolysis: diagnostic vs. therapeutic ultrasound. Ultrasound Med Biol 2001;27:1683–1689.

14 Daffertshofer M, Gass A, Ringleb P, Sitzer M, Sliwka U, Els T, Sedlaczek O, Koroshetz WJ, Hennerici MG: Transcranial low-frequency ultrasound-mediated thrombolysis in brain ischemia: increased risk of hemorrhage with combined ultrasound and tissue plasminogen activator: results of a phase II clinical trial. Stroke 2005;36:1441–1446.

15 Schneider F, Gerriets T, Walberer M, Mueller C, Rolke R, Eicke BM, Bohl J, Kempski O, Kaps M, Bachmann G, Dieterich M, Nedelmann M: Brain edema and intracerebral necrosis caused by transcranial low-frequency 20-kHz ultrasound: a safety study in rats. Stroke 2006;37:1301–1306.

16 Reinhard M, Hetzel A, Kruger S, Kretzer S, Talazko J, Ziyeh S, Weber J, Els T: Blood-brain barrier disruption by low-frequency ultrasound. Stroke 2006;37:1546–1548.

17 Fatar M, Stroick M, Griebe M, Alonso A, Hennerici MG, Daffertshofer M: Brain temperature during 340-kHz pulsed ultrasound insonation: a safety study for sonothrombolysis. Stroke 2006;37:1883–1887.

18 Reuter P, Masomi J, Kuntze H, Fischer I, Helling K, Sommer C, Alessandri B, Heimann A, Gerriets T, Marx J, Kempski O, Nedelmann M: Low-frequency therapeutic ultrasound with varied duty cycle: effects on the ischemic brain and the inner ear. Ultrasound Med Biol 2010;36:1188–1195.
19 Saguchi T, Onoue H, Urashima M, Ishibashi T, Abe T, Furuhata H: Effective and safe conditions of low-frequency transcranial ultrasonic thrombolysis for acute ischemic stroke: neurologic and histologic evaluation in a rat middle cerebral artery stroke model. Stroke 2008;39:1007–1011.
20 O'Donnell MJ, Xavier D, Liu L, Zhang H, Chin SL, Rao-Melacini P, Rangarajan S, Islam S, Pais P, McQueen MJ, Mondo C, Damasceno A, Lopez-Jaramillo P, Hankey GJ, Dans AL, Yusoff K, Truelsen T, Diener HC, Sacco RL, Ryglewicz D, Czlonkowska A, Weimar C, Wang X, Yusuf S, INTERSTROKE Investigators: Risk factors for ischaemic and intracerebral haemorrhagic stroke in 22 countries (the INTERSTROKE study): a case-control study. Lancet 2010;376:112–123.
21 Koizumi J, Yoshida Y, Nakazawa T, Ooneda G: Experimental studies of ischemic brain edema I. A new experimental model of cerebral embolism in rats in which recirculation can be introduced in the ischemic area. Jpn J Stroke 1986;8:1–8.
22 Menzies SA, Hoff JT, Betz AL: Middle cerebral artery occlusion in rats: a neurological and pathological evaluation of a reproducible model. Neurosurgery 1992;31:100–106.
23 Korninger C, Collen D: Studies on the specific fibrinolytic effect of human extrinsic (tissue-type) plasminogen activator in human blood and in various animal species in vitro. Thromb Haemost 1981;46:561–565.
24 Swanson RA, Morton MT, Tsao-Wu G, Savalos RA, Davidson C, Sharp FR: A semiautomated method for measuring brain infarct volume. J Cereb Blood Flow Metab 1990;10:290–293.
25 Lu A, Clark JF, Broderick JP, Pyne-Geithman GJ, Wagner KR, Khatri P, Tomsick T, Sharp FR: Mechanical reperfusion is associated with post-ischemic hemorrhage in rat brain. Exp Neurol 2009;216:407–412.
26 Zhang L, Zhang ZG, Zhang RL, Lu M, Krams M, Chopp M: Effects of a selective CD11b/CD18 antagonist and recombinant human tissue plasminogen activator treatment alone and in combination in a rat embolic model of stroke. Stroke 2003;34:1790–1795.
27 Sare GM, Geeganage C, Bath PM: High blood pressure in acute ischaemic stroke – broadening therapeutic horizons. Cerebrovasc Dis 2009;27(suppl 1):156–161.
28 Gautier S, Petrault O, Gele P, Laprais M, Bastide M, Bauters A, Deplanque D, Jude B, Caron J, Bordet R: Involvement of thrombolysis in recombinant tissue plasminogen activator-induced cerebral hemorrhages and effect on infarct volume and postischemic endothelial function. Stroke 2003;34:2975–2979.
29 Apfel RE, Holland CK: Gauging the likelihood of cavitation from short pulse, low-duty cycle diagnostic ultrasound. Ultrasound Med Biol 1991;17:179–185.
30 Azuma T, Kawabata K, Umemura S, Ogihara M, Kubota J, Sasaki A, Furuhata H: Bubble generation by standing wave in water surrounded by cranium with transcranial ultrasonic beam. Jpn J Appl Physics 2005;44:4625–4630.

MOLECULAR IMAGING AND BIOLOGY

Mol Imaging Biol (2011)
DOI: 10.1007/s11307-011-0511-5

RESEARCH ARTICLE

Cross-validation of Input Functions Obtained by $H_2{}^{15}O$ PET Imaging of Rat Heart and a Blood Flow-through Detector

Nobuyuki Kudomi,[1,2] Hannu Sipilä,[1] Anu Autio,[1] Vesa Oikonen,[1] Heidi Liljenbäck,[1,3] Miikka Tarkia,[1] Jarno Laivola,[1] Jarkko Johansson,[1] Mika Teräs,[1] Anne Roivainen[1,3]

[1]*Turku PET Centre, University of Turku and Turku University Hospital, Turku, Finland*
[2]*Department of Medical Physics, Faculty of Medicine, Kagawa University, Kagawa, Japan*
[3]*Turku Center for Disease Modeling, University of Turku, Turku, Finland*

Abstract

Purpose: Positron emission tomography (PET) with ^{15}O-labeled water ($H_2{}^{15}O$) facilitates the visualization and quantification of blood flow in clinical investigations and also in small animals. The quantification of blood flow requires an input function, which is generally obtained by measuring radioactivity in arterial blood withdrawn during PET scanning. However, this approach is not always feasible, because abundant blood sampling may affect the physiological process being measured. The purpose of the present study was to develop and cross-validate two methods, namely, a blood- and an image-based method for obtaining the input function for blood flow studies from rat $H_2{}^{15}O$ PET.

Methods: The study material consisted of two separate groups of rats. Group 1 rats were imaged twice by a high-resolution research tomograph PET camera at resting condition for a test–retest study (n=4), and group 2 rats were imaged with and without adenosine infusion for a rest–stress study (n=4). In group 1, radioactivity concentration in arterial blood was measured with a new flow-through detector during imaging and a blood-based input function was obtained. The image-based input function was estimated using time-activity curves from the left ventricle and myocardial regions. To validate the two input function methods, myocardial blood flow (MBF) and cerebral blood flow (CBF) were computed, and the methods were tested for reproducibility (test–retest study) and changes (rest–stress study).

Results: The blood- and image-based input functions were similar, and the corresponding CBF values differed only by −6.9±8.1%. In the test–retest study, both MBF and CBF showed good reproducibility, and in the rest–stress study, adenosine significantly increased both MBF (P=0.035) and CBF (P=0.029), compared with the resting condition.

Conclusion: It is possible both to measure the input function from rat *arteria femoralis* during $H_2{}^{15}O$ PET imaging and to estimate the input function from rat $H_2{}^{15}O$ PET images, thereby facilitating the assessment of blood flow in organs visible in PET images.

Key words: Small animal, $H_2{}^{15}O$, PET, Input function

Introduction

The quantification of blood flow in organs, such as the brain, heart, liver, kidney, and skeletal muscle, has the potential to provide information regarding patho-physiological processes in those organs. In addition, measurements of blood flow in small animals, such as rats, may be helpful for pre-clinical studies related to drug discovery and development [1–3]. Positron emission tomography (PET) imaging with ^{15}O-labeled water ($H_2{}^{15}O$) facilitates quantitative

Correspondence to: Nobuyuki Kudomi; *e-mail:* kudomi@med.kagawa-u.ac.jp

Published online: 03 August 2011

measurement of blood flow, using tracer kinetic modeling. The computation of such quantitative images requires the notion of the time variation of radiotracer concentrations in the organ tissue and in the blood entering the organ, in other words, an input function.

In general, the input function is obtained by measuring the radioactivity of arterial blood samples withdrawn during PET imaging; however, this approach may not be feasible for small animals [3] because abundant blood sampling can affect the physiological process we intend to measure [4]. To minimize the amount of blood withdrawn from a small animal, a microfluidic blood sampler device has been developed [5]. Using this device, the amount of blood needed for input measurements can be reduced to less than 5% of the total blood volume of the animal. However, when assessing changes in blood flow due to, for example, pharmacological stress, multiple scans are required (at rest and under stress) and the total volume of blood for input measurements will increase significantly. Furthermore, with regards to studies with $H_2{}^{15}O$, it may not be easy to measure radioactivity concentration from frequent samples because the physical half-life of ^{15}O is very short (122.24 s).

Thus, a method for obtaining the input function without frequent blood sampling, or even eliminating the need for blood sampling, would be valuable. One solution for avoiding frequent blood sampling and measuring is to make an arteriovenous shunt, as demonstrated previously in studies using 2-deoxy-2-[^{18}F]fluoro-D-glucose (^{18}F-FDG) and $H_2{}^{15}O$ [6, 7]. Another solution is to extract the input function from blood pool, for example, from a dynamic PET image of heart cavity. Recently, Fang and Muzic reported on a method for obtaining the input function from ^{18}F-FDG PET images of rat and mouse heart [8]. Subsequently, we developed a method for extracting the input function from rat ^{18}F-FDG PET images [9] for wider use by introducing a model function that reflects various physiological and experimental conditions. Both of these ^{18}F-FDG input function methods are characterized by the simultaneous fitting of left ventricle (LV) and myocardium (Myo) time-activity curves (TAC) and correction for partial volume effect (PVE). The idea to correct for PVE from LV and Myo TACs was originally developed by Iida and co-workers for their studies of human myocardial blood flow (MBF) [10].

In the present study, we obtained a blood-based input function from rat *arteria femoralis* by using a new flow-through detector developed in our laboratory, which required a new type of dispersion correction, as compared with the previously developed method. We also estimated an image-based input function from LV and Myo TACs by using high-resolution research tomograph (HRRT). The validity of the obtained input functions was tested by computing the MBF and cerebral blood flow (CBF) values in test–retest and rest–stress settings.

Materials and Methods

Synthesis of $H_2{}^{15}O$

The ^{15}O isotope was produced with Cyclone 3 Cyclotron (IBA Molecular, Belgium) by the $^{14}N(d,n)^{15}O$ nuclear reaction on natural nitrogen gas. When the nitrogen target gas contains 1% oxygen gas, ^{15}O isotope is recovered at the target output as $^{15}O_2$ gas [11, 12]. The $^{15}O_2$ and H_2 gases were processed into water vapor in an oven at 700°C. Radiowater, $H_2{}^{15}O$, was produced in a continuously working water module (Radiowater Generator, Hidex Oy, Turku, Finland) using a diffusion membrane technique to trap the radioactive water vapor into the sterile saline [13]. The $H_2{}^{15}O$ dose (500 μL) was manually withdrawn from Hidex RWG.

Animals and PET Procedures

All animal experiments were approved by the Lab Animal Care and Use Committee of the State Provincial Office of Southern Finland and carried out in compliance with the Finnish laws relating to the conduct of animal experimentation.

Group 1 consisted of four adult male Sprague–Dawley rats (Harlan, The Netherlands; normal; weight, 603±47 g; age, 10–11 months). PET imaging was performed by using an HRRT camera (CPS Siemens, Knoxville, TN) with a spatial resolution of 2.3–3.2 mm in full width at half maximum, sensitivity of 2.5–3.3% and axial field of view of 25.2 cm, which allows imaging of the whole rat [14]. For PET imaging, all rats were anesthetized with isoflurane (induction, 3% and maintenance, 2.2%) and placed on a warm pallet. Two catheters were inserted; one in the tail vein for tracer injection (24-gauge cannula; BD Neoflon, Becton Dickinson Infusion Therapy AB, Helsingborg, Sweden) and the other in *arteria femoralis* (PE—i.d., 0.5 mm and o.d., 0.8 mm; the blood vessel was clamped around the tubing by ligation) for the measurement of blood radioactivity. The blood sampling tube was installed through a flow-through multi-wire proportional counter constructed in our laboratory [15]. The detector was cross-calibrated with the PET camera via an ion chamber. A peristaltic pump was used for blood flowing. Blood flow rate through the detector was adjusted at 500 μL/min. After a transmission scan for attenuation correction, $H_2{}^{15}O$ (50 MBq and 500 μL) was intravenously injected as a bolus via the tail vein. Subsequent flushing with saline was omitted because it causes a double input peak (unpublished data). Dynamic imaging for 120 s and measurement of blood radioactivity started at the time of injection. After 20 min, when ^{15}O from the first tracer injection had decayed, a second $H_2{}^{15}O$ (50 MBq) bolus was injected and dynamic imaging for 120 s was performed in resting condition thereby establishing the test–retest setting.

Group 2 consisted of four adult male Sprague–Dawley rats (normal; weight, 333±57 g; age, 2–4 months). All rats were anesthetized with isoflurane; the tail veins were catheterized for tracer injection; and dynamic $H_2{}^{15}O$ (50 MBq and 500 μL) imaging for 120 s was performed as described above, with the

exception that the study was carried out without blood sampling. The first imaging was performed at rest and the second imaging under a pharmacological stress condition (120 μg $min^{-1} \cdot kg^{-1}$ adenosine infusion) thereby establishing the rest–stress setting.

Data Processing and Analysis

PET data were reconstructed using the ordinary Poisson ordered-subsets expectation maximization 3D algorithm (eight full iterations and 16 subsets) with attenuation correction into dynamic 15×2, 10×3, and 12×5 s frames. A reconstructed image had 37 frames and 256×256×207 matrix size with a pixel size of 1.22×1.22 and 1.22 mm. Images were post-smoothed with a 2-mm kernel 3D Gaussian filter. Kernel size was chosen on the basis of spatial resolution measurement with a point source in air [14]. The resulting spatial resolution is approximately 2.5 mm in radial, tangential, and axial directions.

Region of interest (ROI) was drawn on the LV region in a summed image (Fig. 1, left side). Then, the reconstructed dynamic image was summed for the first and second halves of imaging, namely from 0 to 60 s and from 60 to 120 s, respectively, and an image for drawing the Myo region was generated by subtracting the first half from the second-half summed images after normalizing the two images divided by the values of LV ROI in the corresponding images (Fig. 1, right side). In group 1, the sizes of the LV and Myo ROIs were 0.089±0.040 and 0.66±0.18 cm^3, respectively, and correspondingly in group 2, 0.066±0.015 and 0.45±0.13 cm^3, respectively. The LV and Myo TACs were extracted from the dynamic image. Then, the input function was estimated by the method previously developed for human MBF study using the obtained LV and Myo TACs (see Appendix A) [10], and the MBF value was computed simultaneously. For validation by comparison with CBF values, ROIs on whole brain were also drawn for each animal and brain TACs were extracted accordingly.

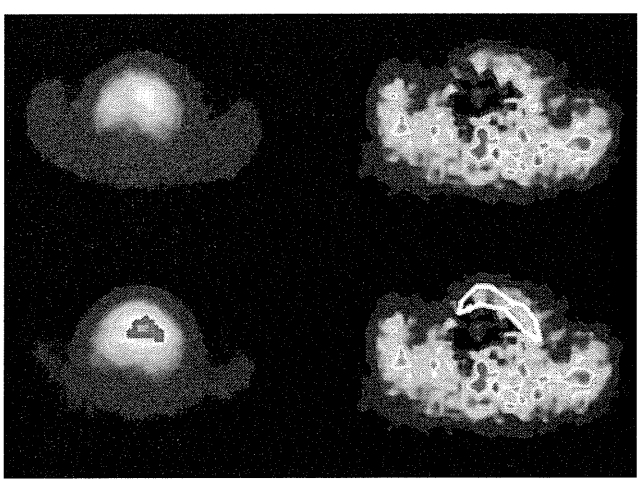

Fig. 1. Representative axial view of a slice of the heart region generated by summing all frames (*left*) and by subtracting the first from the second half frames (*right*) and ROIs drawn on the LV (*lower left*) and Myo regions (*lower right*).

To obtain the blood-based input function, the measured blood curve was corrected for dispersion (see Appendix B) and the delay time between the brain and detector sensitive regions [16].

The CBF values were calculated with a one-tissue compartment model using the blood- and image-based input functions and the Gauss–Newton optimization algorithm. The MBF value was also calculated using the blood-based input with Eqs. 1 and 2 and the Gauss–Newton optimization algorithm.

Statistical Analyses

All the results are expressed as the mean±standard deviation (SD). The correlations between the CBF values computed by using either the blood- or image-based input function were evaluated using linear regression and Pearson's correlation coefficient. The Bland–Altman method was applied to analyze the differences observed in the MBF and CBF values with either the blood- or image-based input function. The paired t test was applied to the intra-animal comparison of the MBF and CBF values between test and retest imaging and between rest and stress imaging. A P value of less than 0.05 was considered statistically significant. All statistical analyses were conducted using the Grace environment (http://plasma-gate.weizmann.ac.il/Grace/).

Results

The blood- and image-based input functions appeared to be very similar when dispersion correction was applied (Fig. 2). When using the image-based input function, the estimated α and β values were 0.40±0.14 (range, 0.17–0.68) and 0.53±0.10 (range, 0.42–0.58), respectively. Figure 3 shows representative whole-brain radioactivity curves for rest–rest and rest–stress studies. The correlations between the MBF values and between the CBF values computed by using the blood- *versus* image-based input functions are shown in Fig. 4. The regression lines were $y=0.13+0.66\,x$ ($r=0.81$; $P<0.01$) and $y=0.10+0.90x$ ($r=0.88$; $P<0.005$) for MBF and CBF, respectively. For CBF, the slope was close to unity, which indicates a strong correlation between the methods. Differences in MBF and CBF values between the blood-based and image-based input functions were −2.7±8.8% and −6.9±8.1%, respectively. According to the t test, these differences in the MBF and CBF values were not statistically significant.

In order to assess the agreement between the two methods, the Bland–Altman plot was applied for the calculated MBF and CBF values. The results are shown in Fig. 5, demonstrating a −0.009 and −0.04 mL min^{-1} g^{-1} bias, respectively, from the blood-based to the image-derived input function methods.

Table 1 summarizes the MBF and CBF values obtained during rest and stress conditions for groups 1 and 2. The test–retest setting (rest–rest) showed good reproducibility for both MBF and CBF values between the first and second scans in group 1. In group 2 with the rest–stress setting, both MBF and CBF values in stress were significantly higher in

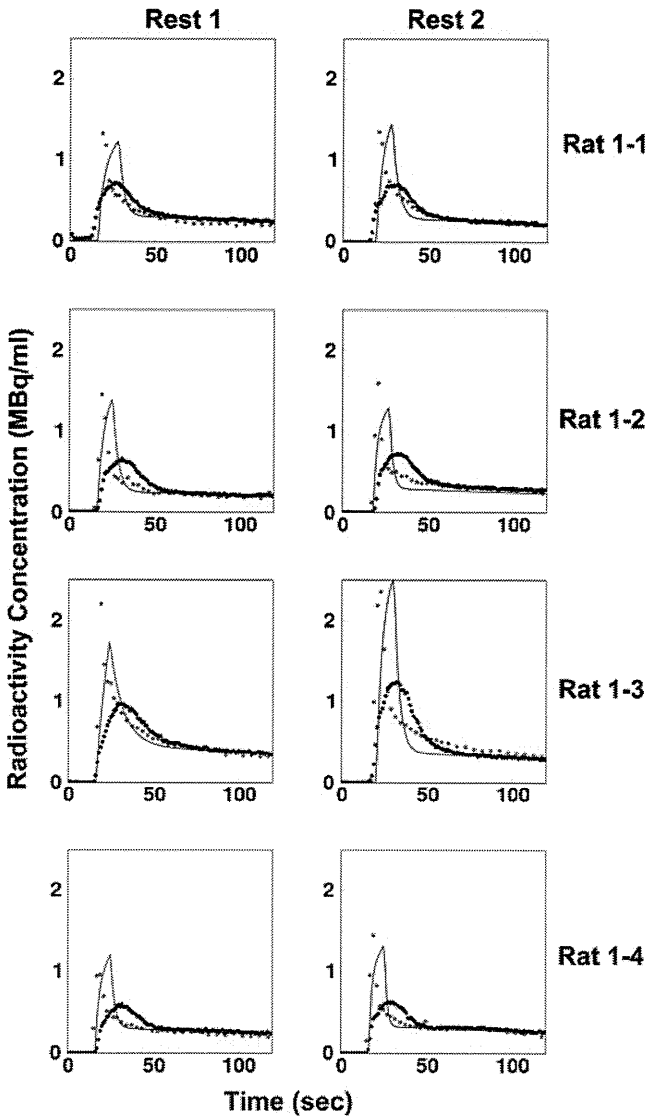

Fig. 2. Comparison of image-based input functions (*red dots*), blood-based input functions with (*blue line*), and without (*black dots*) dispersion correction in group 1 experiments.

comparison to values in rest, namely, P=0.035 and 0.029, respectively.

Discussion

This study reports on the cross-validation of input functions obtained either by measuring the radioactivity of rat arterial blood or by estimating the input function from $H_2{}^{15}O$ PET images of rat heart. The imaging was performed by using an animal/human-brain PET camera (HRRT). The cross-validation was tested by comparing the MBF and CBF values obtained by the two different methods, and also by comparing the MBF and CBF values obtained in test–retest setting or differing (rest–stress) physiological conditions. The mean differences in the MBF and CBF values between the blood-based and image-based input functions were −2.7±8.8% and −6.9±8.1%, respectively. For test and retest imaging, no significant difference was found in MBF and CBF between test and retest imaging. The MBF values for rest and stress conditions were 0.37±0.01 and 0.52±0.08, and the corresponding CBF values were 0.70±0.13 and 0.94±0.04, respectively, and the differences were statistically significant (P=0.035 and 0.029, respectively). Our results suggest that the two methods, namely, estimating the input function from PET images and measuring the input function by using a system consisting of a peristaltic pump, proportional counter, and continuous blood sampling during the scanning, are feasible for the assessment of MBF, CBF, and blood flow in other organs without affecting the physiological status of the animal as a result of abundant blood sampling.

For the purposes of imaging small animals, some sites have recently introduced small-animal PET scanners [2]; however, they do not allow blood flow studies with $H_2{}^{15}O$ unless there is a cyclotron available for providing the tracer $H_2{}^{15}O$, which has a very short half-life of 122.24 s (for comparison, ^{18}F-FDG has a longer half-life of about two hours so it can be transported from a separate cyclotron facility). The present study was carried out using an animal/human-brain PET camera placed in close proximity to the

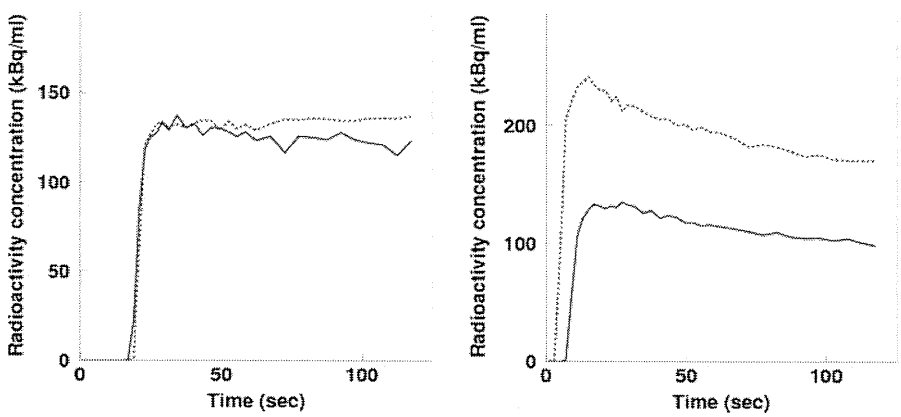

Fig. 3. Representative whole-brain radioactivity curves for *left*: rest (*solid line*) *versus* rest (*dashed line*) and *right*: rest (*solid line*) *versus* stress (*dashed line*) studies.

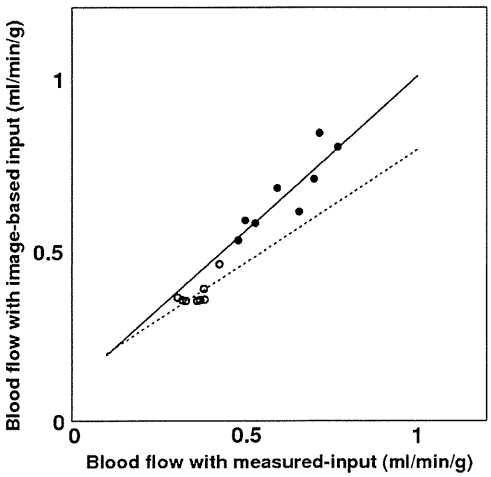

Fig. 4. Linear regressions depicting the correlation between the MBF (*white circles*) values and between the CBF values (*black circles*) calculated by using the blood-based input function (*x*-axis) and image-based input function (*y*-axis). The *solid line* shows the regression for CBF: $y=0.10+0.90x$ ($r=0.88$; $P<0.005$) and *dashed line* for MBF: $y=0.13+0.66x$ ($r=0.81$; $P<0.01$).

production of $H_2{}^{15}O$. Nevertheless, we believe the present method would be feasible for studies with small-animal PET/CT scanners as long as the target organ and LV can be scanned simultaneously.

The present method for estimating the input function from PET images is characterized by a correction for spillover and PVE using two TACs, namely for LV and Myo. The effects are caused by the vascular radioactivity being blurred into adjacent tissues and outer region, and *vice versa*, and also, cardiac and respiratory motion creates an additional mixture between vascular structures and surrounding tissues. The method of deriving input functions by correcting for such effects from the two TACs was firstly introduced by Iida *et al.* [10] in a MBF study in human subjects (Appendix A). The obtained equation was expressed as measured LV and Myo terms as well as parameters representing blood flow, blood volume, and mixing coefficients, and the input function was estimated by optimizing these parameters. Unlike their approach, we did not introduce blood volume data from measurement with $C^{15}O$ scan, instead, it was simultaneously estimated in the optimization procedure. Also, we did not separate regions between LV and right ventricle because this is not practical for small animal studies due to the spatial resolution (Fig. 1). Still, as shown in Figs. 2 and 4, the inputs were quite similar to the blood-based input, and a tight correlation ($y=0.10+0.90x$, $r=0.88$; $P<0.005$) was found in CBF between the image- and blood-based inputs, suggesting that the present method without blood volume data can be used for estimating input for rat. Yee *et al.* have demonstrated an image-based method in which the input function was estimated from a single TAC in LV ROI, assuming the drawn ROI is filled with either arterial blood or tissue [17], and the obtained regression in CBF against their reference was $y=0.14+0.73x$, $r=0.70$.

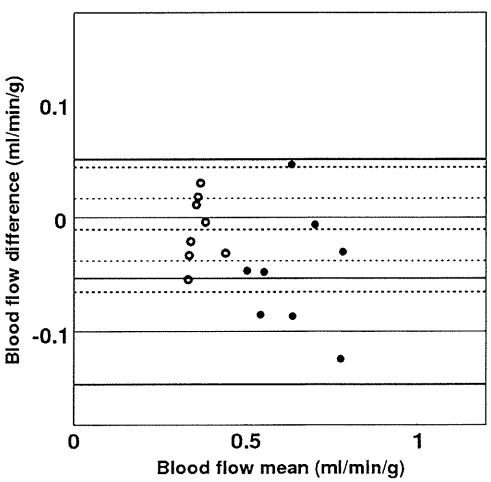

Fig. 5. Bland–Altman plot for difference in CBF (*black circles*) and MBF (*white circles*) between blood- and image-based input function methods, respectively. *Horizontal solid lines* represent mean (*thick line*), SDs (*thin line*), and 2 SDs (*thin line*) for CBF and *dashed lines* represent mean (*thick line*), SDs (*thin line*), and 2SDs (*thin line*) for MBF.

To obtain the blood-based input function, we measured blood radioactivity from rat *arteria femoralis* by using a new flow-through detector developed in our laboratory [15]. In our preliminary study, it was found that a correct input cannot be obtained by the previously developed dispersion correction method [18, 19]. Therefore, we further developed dispersion correction method. In the newly developed correction method, the measured blood curve was corrected by taking into account the transit time in the detector sensitive region, in other words, the effect of a long transit time was estimated by convolving the input model function by a rectangular function with width T_w (s), which corresponds to the transit time. The scale and shape of the blood-based input function were similar to those of the image-based input function. When the measured blood curve was corrected by using the methods previously developed by Iida *et al.* [18] or Munk *et al.* [19], two peaks appeared in the corrected curve and the shape of the input function was not reconstructed. The previous methods assume that the dispersion in blood curve occurs due to the distribution of flowing velocity in tube, *i.e.*, the central part flows faster than the peripheral part, and the apparent effect is expressed by convolution of exponential function [18]. However, in the present measurement set-up, the "dispersion" occurs due to long transit time, and the effect is expressed by a rectangular function in the Eq. 7. Thus, in the present measurement set-up, the method for dispersion correction is more feasible.

An alternative method for obtaining the arterial input function is to use beta probes [20]; however, beta probes may fail in providing accurate input functions unless they are used intravenously, which requires complicated microsurgery [3, 21].

Table 1. Summarized results of the MBF and CBF values (mL min^{-1} g^{-1})

	MBF		MBF		CBF		CBF	
	Image-based input		Blood-based input		Image-based input		Blood-based input	
Group 1—rest–rest study								
Animal	Rest 1	Rest 2	Rest 1	Rest 2	Rest 1	Rest 2	Rest 1	Rest 2
1–1	0.35	0.36	0.37	0.32	0.58	0.61	0.53	0.65
1–2	0.35	0.35	0.33	0.37	0.68	0.58	0.60	0.51
1–3	0.35	0.42	0.32	0.41	0.70	0.53	0.70	0.50
1–4	0.38	0.35	0.38	0.36	0.80	0.84	0.78	0.71
Mean±SD	0.36±0.02	0.37±0.03	0.37±0.03	0.36±0.03	0.68±0.09	0.64±0.14	0.65±0.11	0.59±0.10
Group 2—rest–stress study								
Animal	Rest	Stress			Rest	Stress		
2–1	0.37	0.54			0.78	0.97		
2–2	0.36	0.56			0.74	0.90		
2–3	0.37	0.55			0.51	0.98		
2–4	0.37	0.57			0.78	0.90		
Mean±SD	0.37±0.01	0.52±0.08			0.70±0.13	0.94±0.04		

In group 1 with test–retest setting (rest–rest), the mean MBF and CBF values were very similar for the first and second scans. In group 2 with rest–stress setting, we found a significant increase in both MBF and CBF under adenosine-induced stress, as compared with the resting condition. This finding suggests that our image-based method can be applied to the assessment of changes in rat MBF or CBF, or blood flow in other organs that result from stimulation, such as pharmacological stress.

We computed the CBF values for the rat brain region. The values ranged between 0.5 and 0.8 mL min^{-1} g^{-1} for resting condition, which is in line with previously reported data, ranging from 0.2 to 0.8 [7] and 0.55 mL min^{-1} g^{-1} [17].

In a previous study using $^{13}NH_3$ PET in rat, an increase of MBF under an adenosine-induced stress condition was observed [22], which is in agreement with the result of the present study. Our MBF values were similar under the same condition and within the same group, and the values across the conditions ranged from 0.36 to 0.57 mL min^{-1} g^{-1}; these values were smaller than the previously reported values in the $^{13}NH_3$ PET study, ranging from 3.0 to 7.4 mL min^{-1} g^{-1} [22]. The MBF values are affected by many factors, including anesthesia, rat size, difference of tracer, location of ROI on Myo region, and PVE. As to PVE, the location of Myo ROI affects the MBF more than that of LV, which is not moving and locates on the central part of cardiac image. Further studies are required for obtaining more reliable values regarding MBF. An anatomical drawing tool for LV and Myo could improve this. The present study was intended to obtain input functions for $H_2{}^{15}O$ flow study and the consistency of MBF values between the two methods suggests the input function is well estimated.

An important advantage of $H_2{}^{15}O$ is attributable to the short physical half-life of ^{15}O (122 s), which facilitates repeated scanning with approximately 10-min intervals, as in the present study, as well as scanning with a combination of $H_2{}^{15}O$ and other ligands, such as ^{18}F-FDG. Using ^{18}F-FDG or other ligands, the additional measurement of blood flow in a targeted organ provides important information, for example, the first-pass extraction fraction, which is calculated from a parameter of transport of tracer from blood into tissue and blood flow. In an experiment with small animals, the present method with $H_2{}^{15}O$ and our previous method with ^{18}F-FDG [9] for image-based input would be quite crucial, although the feasibility should first be tested for tracers other than $H_2{}^{15}O$ and ^{18}F-FDG. If either of the present method is applied to another tracer, and especially if the tracer is metabolized into different radiochemical forms, further corrections are needed. This can be done by taking a single blood sample or several samples during the scan for a radiometabolite analysis. Otherwise, the radiometabolite may be mathematically estimated based on a model function, as has been done in $^{15}O_2$ [23–25] and 6-[^{18}]fluoro-L-dopa [23] studies.

For the purpose of assessing CBF in small animals, alternative methods for quantifying CBF include ^{14}C-iodoantipyrine autoradiography [26], hydrogen clearance method [27], and use of beta probes [7, 20, 28]. The ^{14}C-iodoantipyrine autoradiography has a high spatial resolution; however, a disadvantage is the need to kill the animals after the experiment, which prevents serial experiments on the same animal. The hydrogen clearance method yields, in theory, quantitative CBF values with a high temporal resolution, but a relatively low spatial resolution. The beta probe provides an excellent temporal resolution for measuring CBF in small animals; however, the method requires the insertion of a fine probe into brain tissue. The PET with $H_2{}^{15}O$ allows for reasonable spatial and temporal resolutions for the assessment of quantitative CBF and blood flow in other organs as well.

In conclusion, the input functions obtained either by measuring the concentration of $H_2{}^{15}O$ in arterial blood or by estimating from $H_2{}^{15}O$ PET images proved to be feasible for the purpose of assessing blood flow during dynamic PET imaging in rat. The image-based method may be preferable if the same accuracy can be obtained because it eliminates laborious procedures.